AIAA 2004-0554

Transonic Drag Prediction on a DLR-F6 Transport Configuration Using Unstructured Grid Solvers

E. M. Lee-Rausch
N. T. Frink
NASA Langley Research Center
Hampton, Virginia

D. J. Mavriplis
University of Wyoming
Laramie, Wyoming

R. D. Rausch
W. E. Milholen
NASA Langley Research Center
Hampton, Virginia

42nd Aerospace Sciences Meeting and Exhibit
January 5–8, 2004
Reno, Nevada

Transonic Drag Prediction on a DLR-F6 Transport Configuration Using Unstructured Grid Solvers

E. M. Lee-Rausch [*]   N. T. Frink [†]   D. J. Mavriplis [‡]

R. D. Rausch [§]   W. E. Milholen [¶]

Abstract

A second international AIAA Drag Prediction Workshop (DPW-II) was organized and held in Orlando Florida on June 21-22, 2003. The primary purpose was to investigate the code-to-code uncertainty, address the sensitivity of the drag prediction to grid size and quantify the uncertainty in predicting nacelle/pylon drag increments at a transonic cruise condition. This paper presents an in-depth analysis of the DPW-II computational results from three state-of-the-art unstructured grid Navier-Stokes flow solvers exercised on similar families of tetrahedral grids. The flow solvers are USM3D – a tetrahedral cell-centered upwind solver, FUN3D – a tetrahedral node-centered upwind solver, and NSU3D – a general element node-centered central-differenced solver.

For the wing/body, the total drag predicted for a constant-lift transonic cruise condition showed a decrease in code-to-code variation with grid refinement as expected. For the same flight condition, the wing/body/nacelle/pylon total drag and the nacelle/pylon drag increment predicted showed an *increase* in code-to-code variation with grid refinement. Although the range in total drag for the wing/body fine grids was only 5 counts, a code-to-code comparison of surface pressures and surface restricted streamlines indicated that the three solvers were not all converging to the same flow solutions– different shock locations and separation patterns were evident. Similarly, the wing/body/nacelle/pylon solutions did not appear to be converging to the same flow solutions.

Overall, grid refinement did not consistently improve the correlation with experimental data for either the wing/body or the wing/body/nacelle pylon configuration. Although the absolute values of total drag predicted by two of the solvers for the medium and fine grids did not compare well with the experiment, the incremental drag predictions were within ±3 counts of the experimental data. The correlation with experimental incremental drag

was not significantly changed by specifying transition. Although the sources of code-to-code variation in force and moment predictions for the three unstructured grid codes have not yet been identified, the current study reinforces the necessity of applying multiple codes to the same application to assess uncertainty.

Introduction

A concerted international effort is underway through the AIAA Applied Aerodynamics Technical Committee to quantify the uncertainty associated with computing drag from computational fluid dynamics (CFD) methodology. The first attempt culminated with the 1st AIAA Drag Prediction Workshop (DPW-I) held at Anaheim, California June 9-10, 2001.[1-6] All 37 participants from several countries using a variety of Navier-Stokes flow solvers were equally surprised by the outcome– the final standard deviation of computed drag on a simple wing-body transport configuration at a fairly benign transonic cruise condition using each participant's "best" flow solver was quantified in the range of ±21 drag counts.[2] While some obvious shortcomings in the computational grids were identified, the participants eagerly sought a follow-on workshop to further address this large variation in predicted drag.

Two of the current authors along with several other workshop participants initiated an independent follow-on grid convergence study to evaluate the quantitative effects of discretization error on the code-to-code variation of forces and moments for the DLR-F4 configuration.[7] Results for two structured grid codes and two unstructured grid codes were compared for a constant angle-of-attack case near the DPW-I constant cruise lift. The structured grid refinement study was inconclusive because of difficulties computing on the fine grid. The grid refinement study for the unstructured grid codes showed an increase in variation of forces and moments with grid refinement. However, all of the unstructured grid results were not definitively in the range of asymptotic grid convergence. The study indicated that certain numerical schemes or other code-to-code differences may have a larger effect than previously thought on grid sizes considered to be "medium" or "fine" by current standards.

A second international AIAA Drag Prediction Workshop (DPW-II) was subsequently organized and held in Orlando Florida on June 21-22, 2003.[8,9] The primary

[*] Member AIAA, Research Engineer NASA Langley Research Center(LaRC), Hampton, Virginia.

[†] Associate Fellow AIAA, Senior Research Engineer NASA LaRC.

[‡] Associate Fellow AIAA, Professor University of Wyoming, Laramie, Wyoming.

[§] Member AIAA, Research Scientist NASA LaRC.

[¶] Senior Member AIAA, Research Scientist NASA LaRC.

purpose was to 1) investigate the code-to-code uncertainty with more carefully generated grids, 2) address the sensitivity of the drag prediction to grid size, and 3) quantify the uncertainty in predicting nacelle/pylon drag increments at a transonic cruise condition. A similar wing/body (WB) transport was chosen that included a nacelle/pylon component (WBNP). A series of coarse, medium, and fine grids were constructed for both the WB and WBNP configurations using prescribed "best-practice" guidelines for both structured and unstructured solvers. A notable outcome of DPW-II was that the statistical uncertainty of predicting transonic cruise drag significantly decreased over that of DPW-I. The estimated code-to-code population standard deviations of total drag for the nested solutions was ±7.3 counts for the WB, ±11.4 counts for the WBNP and ±8 counts for the nacelle/pylon increment.[10] The grid resolution studies were also useful, but still led to a consensus that many of the provided grids were not adequate. The truth of the phrase "grids are everything" was continually reinforced during DPW-II.

The intent of this paper is to capitalize on the unique opportunity afforded by DPW-II to present more in-depth analysis of three distinctly different unstructured Navier-Stokes flow solvers exercised on a similar family of tetrahedral grids. The flow solvers are USM3D[11] – a tetrahedral cell-centered upwind solver, FUN3D[12] – a tetrahedral node-centered upwind solver, and NSU3D[13] – a general element node-centered central-differenced solver. A total of twelve tetrahedral grids were generated for each flow solver from the VGRIDns code using common surface input files for the WB and WBNP. Grid densities were altered by changing a global scaling factor. Six of the node-based grids were further decomposed into prism elements within the viscous layers for the NSU3D code. This paper will primarily examine the grid sensitivities and code-to-code comparisons for absolute and incremental drag on the DPW-II configuration between the three codes.

Test Configuration and Data

The DLR-F6 is derived from the DLR-F4 configuration which was the focus of the DPW-I.[1] The DLR-F6 represents a twin-engine wide-body aircraft and has also been the focus of several wind tunnel tests and computational studies. Multiple engine geometries and installation locations were tested.[14] However, only one geometry and installation location are considered for this workshop (CFM56-long, position 1). The design cruise Mach number for the DLR-F6 is $M_\infty = 0.75$, and the lift coefficient is $C_L = 0.500$. The aspect ratio is 9.5 and the leading edge sweep is 27.1°. The engines are represented by flow-through nacelles which are axis-symmetric in shape. The computational geometry

defined by the DPW-II committee is used as the surface definition for all computational grids.[8] The experimental data used for comparison in this paper were also provided by the DPW-II organizing committee.[8]

Flow Solvers

Three unstructured-grid Reynolds averaged Navier-Stokes (RANS) CFD codes are employed in this study: USM3D is a cell-centered code, and NSU3D and FUN3D are node-centered codes.

Cell-Centered Code

USM3D is a tetrahedral cell-centered, finite volume Euler and Navier-Stokes solver[11] within the NASA TetrUSS system.[15] The inviscid flux quantities are computed across the cell faces using the Roe's flux-difference splitting scheme with or without flux limiting, and the spatial discretization is accomplished by an analytical reconstruction process. The full viscous terms are solved with a central-difference stencil. Flow solutions are advanced in time to steady state using an implicit backward-Euler time-stepping scheme. In addition to standard boundary conditions, a number of special boundary conditions are available such as jet inflow/exhaust with swirl, propeller/rotors, blunt trailing edge treatment, and wall function. All USM3D computations presented in this paper are performed fully turbulent with no flux limiter using the wall-function and thick trailing-edge boundary conditions.

A brief note is offered regarding the thick trailing-edge boundary condition. The VGRIDns grid generator does not presently support the generation of thin-layered tetrahedral field cells for resolving the wake flow behind a wing trailing edge. Thus, it is difficult to enforce adequate grid resolution downstream of the trailing edge without resorting to excessive numbers of cells. A special boundary condition has been developed to mimic the relieving effect of a blunt-base wake on a coarse grid, which is useful for cases where the wing has a thick trailing edge. The approach is to introduce a solution-defined transpiration velocity on the blunt-base boundary faces to provide a smooth departure of the flow past the corner. This boundary condition has been well tested over the past decade and is used extensively in USM3D with inviscid flows and wall function applications.

Node-Centered Codes

NSU3D and FUN3D are finite-volume methods in which the flow variables are stored at the vertexes of the mesh. NSU3D solves the equations on mixed element grids including tetrahedra, pyramids, prisms, and hexahedra while FUN3D is currently limited to tetrahedra only for turbulent flows.

FUN3D[12,16,17] employs an implicit upwind algorithm in which the inviscid fluxes are obtained with a flux-

difference-splitting scheme and the viscous terms are evaluated with a finite-volume formulation, which is equivalent to a Galerkin type of approximation for these terms. This formulation results in a discretization of the full Navier-Stokes terms without any thin-layer approximations for the viscous terms. At interfaces delimiting neighboring control volumes, the inviscid fluxes are computed using a Roe-Riemann solver based on the values on either side of the interface. For second-order accuracy, interface values are obtained by extrapolation of the control volume centroidal values, based on gradients computed at the mesh vertexes using an unweighted least-squares technique. The solution at each time-step is updated with a backwards Euler time-differencing scheme. At each time step, the linear system of equations is approximately solved with either a point implicit procedure or an implicit line relaxation scheme.[18] Local time-step scaling is employed to accelerate convergence to steady-state.

NSU3D[13] includes two options for the discretization of the inviscid convective terms. The first option employs a Roe-Riemann solver at control volume interfaces, with a least squares gradient reconstruction procedure for second-order accuracy, similar to the FUN3D discretization. The second option employs centrally differenced convective terms with added matrix-based artificial dissipation. Second-order accuracy is achieved by formulating these dissipative terms as an undivided bi-harmonic operator, which is constructed as two passes of a nearest neighbor Laplacian operator. In the matrix form, this dissipation is similar to that produced by the Riemann solver gradient based reconstruction technique, and is obtained by replacing the difference in the reconstructed states on each side of the control volume interface by the undivided differences along mesh edges resulting from the biharmonic operator construction. In both cases, these differences are then multiplied by the characteristic matrix to obtain the final dissipative terms. The matrix dissipation formulation is used exclusively in this study. The thin-layer form of the Navier-Stokes equations is employed in all cases, and the viscous terms are discretized to second-order accuracy by finite-difference approximation. The basic time-stepping scheme is a three-stage explicit multistage scheme. Convergence is accelerated by a local block-Jacobi preconditioner in regions of isotropic grid cells. In boundary layer regions, where the grid is highly stretched, a line preconditioner is employed.[19] An agglomeration multigrid algorithm is used to further enhance convergence to steady-state. The Jacobi and line preconditioners are used to drive the agglomeration multigrid algorithm, which results in a rapidly converging solution technique.

Turbulence Model

For the current study, the one-equation turbulence model of Spalart and Allmaras is used.[20] USM3D, NSU3D and FUN3D employ the version of SA referred to as SA-Ia. This is the version of the model that is given in Spalart and Allmaras,[20] and will be referred to simply as "SA" from now on. For FUN3D and NSU3D, transition is specified by zeroing out the production terms in the turbulence model.

Computational Grids

Two sets of tetrahedral grids were generated for the current study: grids for the cell-centered solver with wall-functions and grids for the node-centered solvers with integration to the wall. Overall spatial resolution is determined by the number of cells (unknowns) for a cell-centered solver and by the number of nodes (unknowns) for a node-centered solver. Additionally, for the grid convergence study with each solver type, two families of coarse, medium and fine grids were generated for the WB configuration and the WBNP configuration. Although the DLR-F6 test configuration was a full span model, the computations were performed on half-models since the flow conditions were symmetric. Figures 1 and 2 show the WB and WBNP surface mesh for the cell-centered and node-centered medium grids.

All of the grids were generated with the VGRIDns advancing-layer and advancing-front grid generation software package.[21,22] The grids generated with VGRIDns were fully tetrahedral. However, VGRIDns uses an advancing layer technique to generate the boundary layer portion of the grid so that prisms can be reconstructed in the boundary layer for use with NSU3D. In the boundary layer, three tetrahedral cells are combined to make up one prism. The mixed-element grids have the same number of nodes (unknowns) and nodal spacing as the fully tetrahedral grids although the number of cells and the shape of the control volume differ in the boundary layers. To streamline the current discussion, only the fully tetrahedral node-centered grids will be discussed in detail.

VGRIDns has two types of spacing requirements: the "inviscid" spacing distributions are used in the advancing-front region of the mesh, and the "viscous" spacing distributions are used in the advancing-layer regions of the mesh where high stretching is required. All WB grids share the same surface definitions and the same underlying inviscid spacing distributions. Similarly, all WBNP grids share the same surface definitions and the same underlying inviscid spacing distributions. The different grids for each configuration were generated by a global coarsening/refinement of the inviscid spacing parameters (VGRIDns "sources") and a global coarsening/refinement of the viscous wall spacing and stretching

**Cell-Centered Medium Grid
3.9M cells**

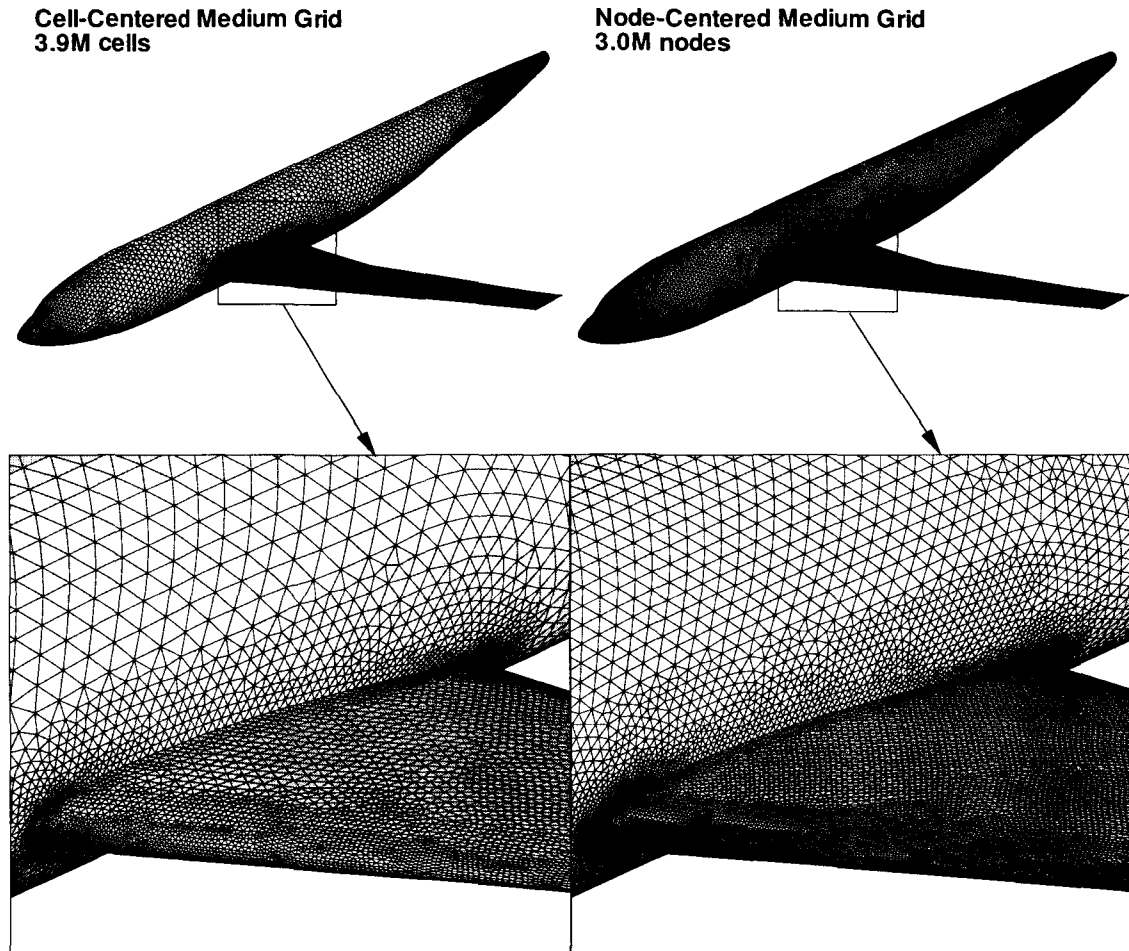**Node-Centered Medium Grid
3.0M nodes**

Fig. 1   Comparison of surface grids for the medium WB grids.

factors. Also, note that the WB and WBNP grids share the same inviscid spacing parameters for the fuselage and wing. Additional "sources" were included in the WBNP grids to accommodate the nacelle and pylon. A comparison of the global grid sizes and spacings for each of the twelve grids is given in Tables 1, 2, 3 and 4.

The medium grids for each family is representative cell-centered and node-centered medium grids. of a "best engineering practices" for the given method with a target wall normal spacing set so that the first point off the wall was located at $y^+ \approx 9$ for the wall-function grids and $y^+ \approx 1$ for the integration to the wall grids. The clustering of points normal to the surface was computed according to the VGRIDns stretching function[5]

$$\delta_n = \delta_1 [1 + r_1(1 + r_2)^{n-1}]^{n-1} \qquad (1)$$

where δ_n is the normal spacing of the nth layer, δ_1 is the spacing of the first layer, and the factors r_1 and r_2 are

constants that determine the rate of stretching. (Note if r_2 is zero the stretching is geometric.) The blunt trailing edges of the wing and nacelles were resolved in all grids. However, the grids are limited to an underlying O-type topology that had no additional resolution of the trailing-edge wake region. The far-field boundary was 106 reference-chord (C_{ref}) lengths away from the surface.

For a given tetrahedral grid, a cell-centered solver and a node-centered solver will have a different number of unknowns. On the same isotropic grid, there are approximately six times the number of cells in a tetrahedral grid as the number of nodes, and the cell-centered control volume sizes will be approximately one-sixth the node-centered control volumes. The control-volume triangular faces for the cell-centered solvers will be approximately one-half of the node-centered dual-volume faces. In order to have comparative WB and

4

Cell-Centered Medium Grid
5.9M cells
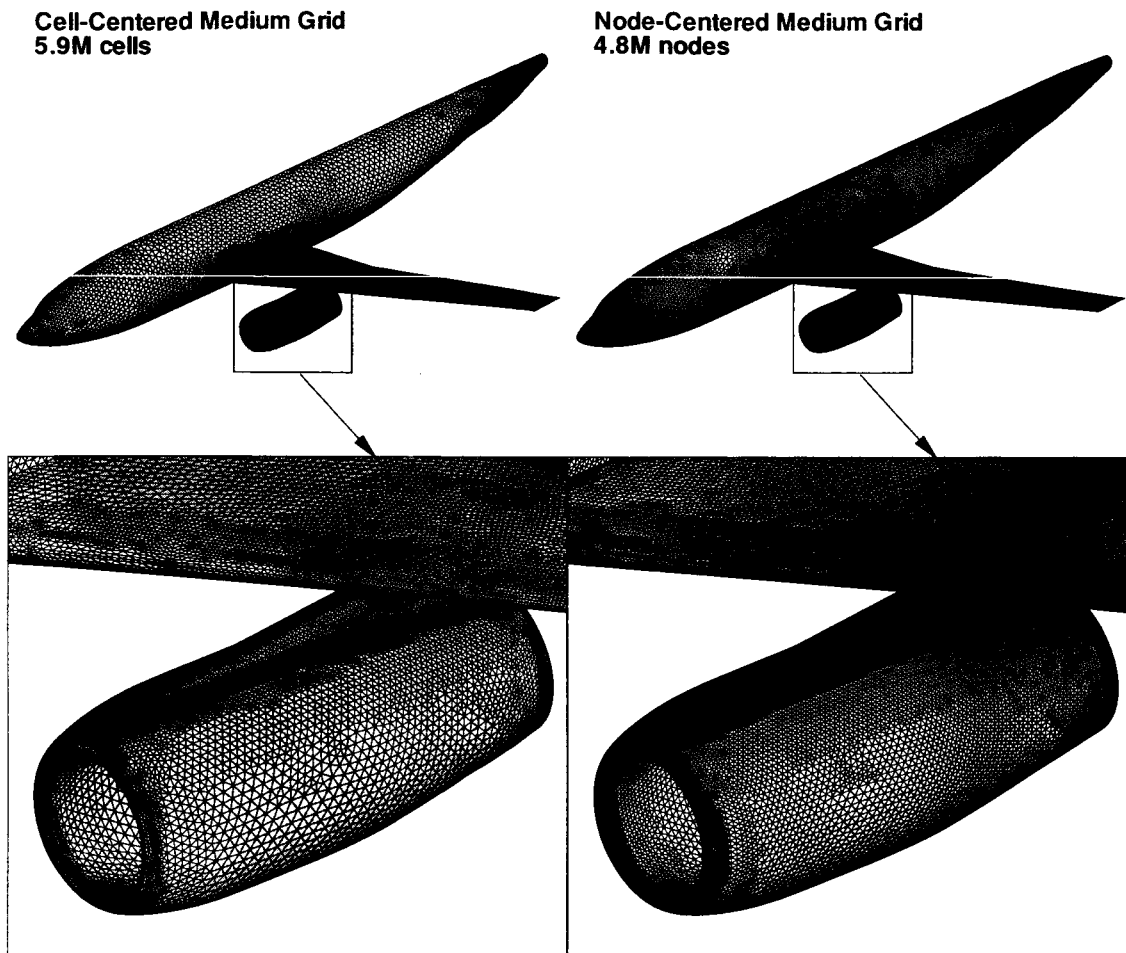
Node-Centered Medium Grid
4.8M nodes

Fig. 2 Comparison of surface grids for the medium WBNP grids.

WBNP grids for both cell-centered and node-centered solvers, the medium node-centered grids were generated by a global refinement of the inviscid spacing parameters of the "best-practices" cell-centered grids – the inviscid spacing parameters of the medium cell-centered grid were all multiplied by 0.66. The viscous spacing parameters were modified for the node-centered grids to accommodate the different turbulence models (wall-function vs. integration to the wall) and the different finite-volume formulation. A comparison of the number of no-slip triangles for the medium grids in Tables 1 and 2 shows that the number of no-slip triangles in the cell-centered grids are half the number in the node-centered grids for the same configuration. Therefore, the cell-centered and node-centered grids have similar surface discretization. However, the total number of cells for the medium cell-centered grids is more than the total number of nodes for the medium node-centered grids even

though the required viscous wall spacings and stretching rates are lower for the node-centered grids. This is due to the fact that the refinement was made to the inviscid spacing parameters or VGRIDns "sources" which act in a localized manner. Figures 1 and 2 shows the overall refinement of the medium grid WB and WBNP surface meshes.

Cell-Centered Solver Grids

The "best-practices" WB cell-centered grid was used for the medium grid solution in the current grid convergence study (see Tables 1 and 3). This grid contained a total of 3,901,658 cells with 49,919 no-slip boundary triangles. The maximum chordwise grid spacing at the wing leading edge was approximately 0.6% local chord, and the maximum chordwise grid spacing at the trailing edge was approximately 0.29% local chord. The blunt wing trailing edge was defined by two cells. Figure 3 shows a comparison of the chordwise spacing across the span of

5

	Cell-Centered Grids			Node-Centered Grids		
	Coarse	Medium	Fine	Coarse	Medium	Fine
Global Spacing Refinement Factor	1.5	1.00	0.67	1	0.66	0.44
Tetrahedral Cells	**1,409,689**	**3,901,658**	**11,347,301**	6,558,758	17,635,283	53,653,279
Tetrahedral Nodes	246,020	675,946	1,954,524	**1,121,301**	**3,010,307**	**9,133,352**
No-Slip Triangles	24,638	49,919	104,180	49,901	109,679	237,121
Cells in Viscous Layer	524,213	1,051,794	2,017,809	3,826,019	8,313,126	22,866,866
Nodes in Viscous Layer	103,973	208,210	404,276	674,338	1,462,475	3,975,437

Table 1   Global grid sizes of WB grids.

	Cell-Centered Grids			Node-Centered Grids		
	Coarse	Medium	Fine	Coarse	Medium	Fine
Global Spacing Refinement Factor	1.5	1.00	0.67	1	0.66	0.495
Tetrahedral Cells	**2,153,501**	**5,912,596**	**16,776,859**	10,715,204	27,875,222	60,412,948
Tetrahedral Nodes	375,728	1,025,010	2,891,082	**1,827,470**	**4,751,207**	**10,278,588**
No-Slip Triangles	43,447	89,678	179,918	89,738	192,785	331,303
Cells in Viscous Layer	909,464	1,877,753	3,494,103	6,871,628	14,614,147	29,535,244
Nodes in Viscous Layer	178,793	367,619	690,072	1,203,608	1,557,848	5,128,216

Table 2   Global grid sizes of WBNP grids.

the wing at the root, crank and tip. The discontinuities in the spacing across the chord is related to the location of surface "patch" edges or divisions which are used in the grid generation process.[22] Spanwise stretching was used along the leading and trailing edges of the wing to reduce the number of cells in areas of low spanwise gradients. The maximum spanwise aspect ratio was approximately 20 for the leading-edge and trailing-edge cells. There was no spanwise stretching at the wing root and tip. The wall normal spacing was set so that the first point off the wall was located at $y^+ \approx 9$ (0.0057 mm model coordinates). The viscous stretching rates r_1 and r_2 were 0.456 and 0.07, respectively. With these parameters, approximately 18 layers were generated in the boundary layer region, where each layer corresponds to a highly stretched triplet of right angle tetrahedra.[22]

The "best-practices" WBNP cell-centered grid was used for the medium grid solution in the current grid convergence study (see Tables 2 and 4). This grid contained a total of 5,912,596 cells with 89,678 no-slip boundary triangles. The same wing spacing parameters described in the previous paragraph were used in the WBNP grid. Also the same viscous wall spacing and stretching rates were used. (Compare Tables 3 and 4.) The maximum chordwise grid spacing at the nacelle leading edge was approximately 0.35% local chord, and the maximum chordwise grid spacing at the trailing edge was approximately 0.34% local chord. The blunt nacelle trailing edge was defined by one cell. Figure 4 shows a comparison of the chordwise spacing around the circumference of the nacelle at 60°, 180° and 300°. (Facing the front of the port nacelle, zero degrees is at the top of the nacelle, and the increasing angle is clock-wise.) As for the wing grid, the discontinuities in the spacing across the chord is related to the location of surface "patch" edges used in the grid generation process. Circumferential stretching was used along the leading and trailing edges of the nacelle to reduce the number of cells in areas of low gradients. The maximum circumferential aspect ratio was approximately 8.5 for the leading-edge and trailing-edge

6

	Cell-Centered Grids			Node-Centered Grids		
	Coarse	Medium	Fine	Coarse	Medium	Fine
Global Spacing Refinement Factor	1.5	1.00	0.67	1	0.66	0.44
% Chordwise Spacing at wing L.E.	0.90	0.60	0.35	0.70	0.45	0.25
% Chordwise Spacing at wing T.E.	0.494	0.29	0.185	0.34	0.33	0.17
Wing T.E. Cells	2	2	2	2	4	6
Ave. Cell y^+	13	9	6	0.9	0.7	0.5
Nominal Boundary Layer Cells	16	18	20	26	26	33
Viscous Wall Spacing δ_1(mm)	0.0855	0.057	0.038	0.00144	0.001	0.000695
Viscous Stretching r_1, r_2	0.456, 0.07	0.456, 0.07	0.456, 0.07	0.2, 0.02	0.2, 0.02	0.13, 0.02
Outer Boundary Box	$106C_{ref}$	$106C_{ref}$	$106C_{ref}$	$106C_{ref}$	$106C_{ref}$	$106C_{ref}$

Table 3   Grid spacings of WB grids.

	Cell-Centered Grids			Node-Centered Grids		
	Coarse	Medium	Fine	Coarse	Medium	Fine
Global Spacing Refinement Factor	1.5	1.00	0.67	1	0.66	0.495
% Chordwise Spacing at nacelle L.E.	0.52	0.35	0.23	0.34	0.15	0.13
% Chordwise Spacing at nacelle T.E.	0.40	0.34	0.15	0.35	0.23	0.17
Nacelle T.E. Cells	1	1	1	1	2	3
Ave. Cell y^+	13	9	6	0.9	0.6	0.5
Nominal Boundary Layer Cells	16	18	20	24	24	28
Viscous Wall Spacing δ_1(mm)	0.0855	0.057	0.038	0.00144	0.001	0.000794
Viscous Stretching r_1, r_2	0.456, 0.07	0.456, 0.07	0.456, 0.07	0.2, 0.02	0.2, 0.02	0.15, 0.02
Outer Boundary Box	$106C_{ref}$	$106C_{ref}$	$106C_{ref}$	$106C_{ref}$	$106C_{ref}$	$106C_{ref}$

Table 4   Grid spacings of WBNP grids.

cells.

A family of WB and WBNP cell-centered grids was generated for the grid convergence study such that the total number of the cells in each mesh differ by a factor of approximately three between the coarse, medium and fine grids. The coarse and fine grids were generated by a global coarsening/refinement of the medium grid spacing parameters (VGRIDns sourcing terms) of 1.5 and 0.67, respectively. The minimum wall spacing between the grids differs by a similar factor. Tables 1 and 2 summarize the global grid sizes for the family of WB and WBNP cell-centered grids, and Tables 3 and 4 illustrate the effect of coarsening and refinement on the chordwise spacings and viscous spacings. Figure 5 compares the chordwise spacing on the upper wing surface at the crank between the coarse, medium and fine grids. Figure 6 compares the chordwise spacing on the exterior nacelle surface at the inboard 60° station. Both figures show a consistent coarsening and refinement of the chordwise spacing on the wing and nacelle. The blunt trailing edge was not refined explicitly due to the use of the USM3D trailing-edge boundary treatment. Although the viscous wall spacings were coarsened/refined, the geometric stretching rates were not modified.
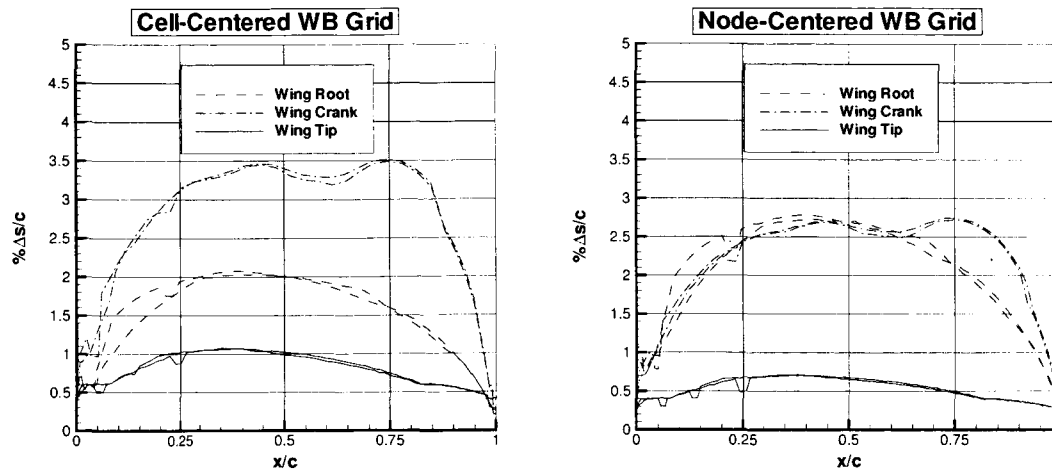
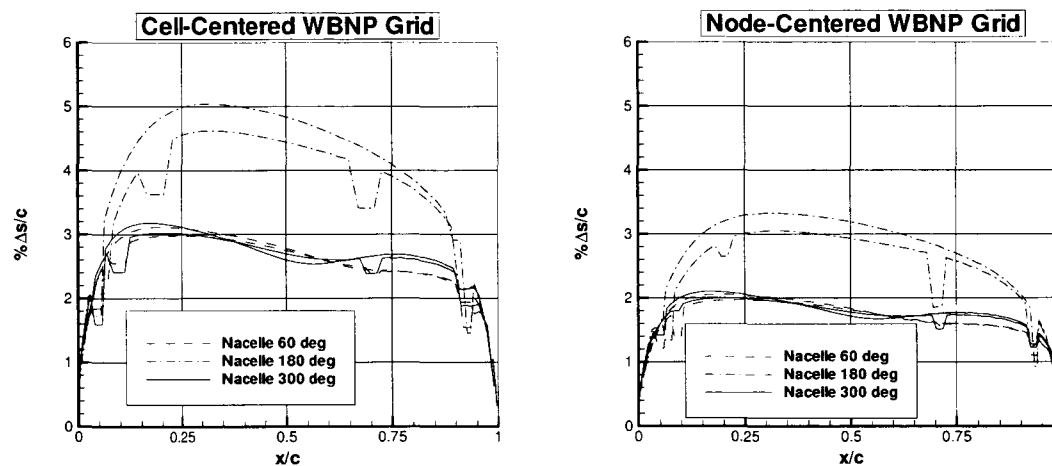Fig. 3 Comparison of chordwise spacing for the medium WB grids across the wing span.

Fig. 4 Comparison of chordwise spacing for the medium WBNP grids around the nacelle.

Node-Centered Solver Grids

The "best-practices" WB node-centered grid was used for the medium grid solution in the current grid convergence study (see Tables 1 and 3). This grid contained a total of 3,010,307 nodes with 109,697 no-slip boundary triangles. The maximum chordwise grid spacing at the wing leading edge was approximately 0.45% local chord, and the maximum chordwise grid spacing at the trailing edge was approximately 0.33% local chord. The blunt wing trailing edge was defined by four cells. Figure 3 shows a comparison of the chordwise spacing across the span of the wing at the root, crank and tip. The maximum chordwise spacing at the root and crank is approximately 2.7% and approximately 1.7% at the tip. Overall, the the chordwise spacing for the node-centered grid is finer

than the cell-centered grid. Spanwise stretching was used along the leading and trailing edges of the wing to reduce the number of cells in areas of low spanwise gradients. The maximum spanwise aspect ratio was approximately 20 for the leading-edge and trailing-edge cells. There was no spanwise stretching at the wing root and tip. The wall normal spacing was set so that the first point off the wall was located at $y^+ \approx 1$ (0.001 mm model scale). The viscous stretching rates r_1 and r_2 were 0.2 and 0.02, respectively. With these parameters, approximately 26 layers were generated in the boundary layer region.

The "best-practices" WBNP node-centered grid was used for the medium grid solution in the current grid convergence study (see Tables 2 and 4). This grid contained a total of 4,751,207 nodes with 192,785 no-slip
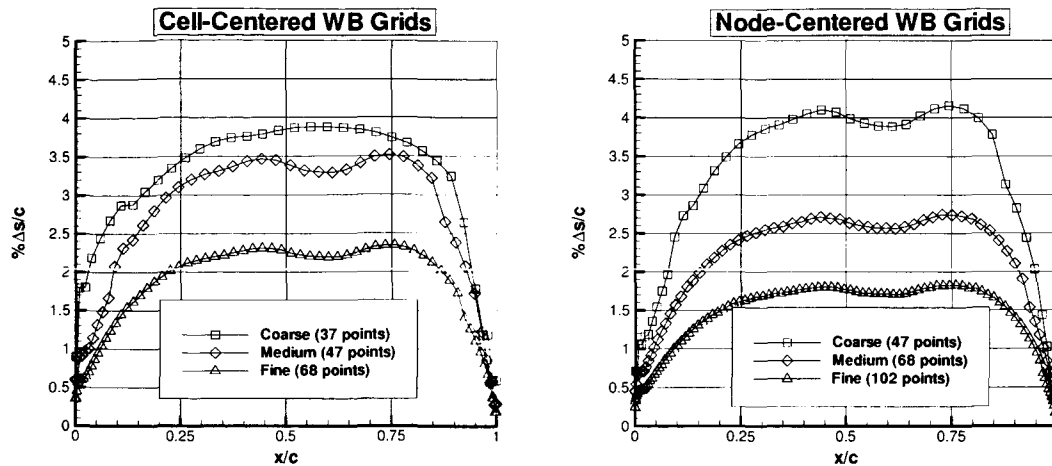
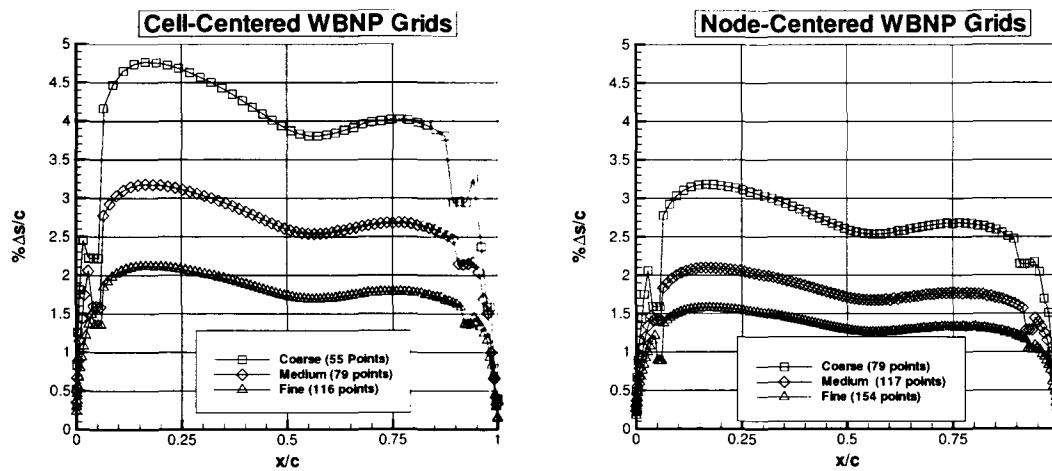Fig. 5 Comparison of chordwise spacing for the WB grids on the upper-wing crank.

Fig. 6 Comparison of chordwise spacing for the WBNP grids on the exterior inboard nacelle.

boundary triangles. The same wing spacing parameters described in the previous paragraph were used in the WBNP grid. Also the same viscous wall spacing and stretching rates were used. (Compare Tables 3 and 4.) The maximum chordwise grid spacing at the nacelle leading edge was approximately 0.15% local chord, and the maximum chordwise grid spacing at the trailing edge was approximately 0.23% local chord. The blunt nacelle trailing edge was defined by two cells. Figure 4 shows a comparison of the chordwise spacing around the circumference of the nacelle at 60°, 180° and 300°. The maximum chordwise spacing is approximately 3.1% at the top of the nacelle and approximately 5.0% at the bottom. Overall, as in the WB case, the chordwise spacing for the node-centered grid is finer than the cell-centered

grid. Circumferential stretching was used along the leading and trailing edges of the nacelle to reduce the number of cells in areas of low gradients. The maximum circumferential aspect ratio was approximately 8.5 for the leading-edge and trailing-edge cells.

A family of WB node-centered grids was generated for the grid convergence study such that the total number of the nodes in each mesh differ by a factor of approximately three between the coarse, medium and fine grids. The WB coarse and fine grids were generated by a global coarsening/refinement of the medium grid spacing parameters (VGRIDns sourcing terms) of 1 and 0.44, respectively. The minimum wall spacing between the grids differs by a similar factor. A family of WBNP grids was designed for the grid convergence study such that the to-

9

tal number of the nodes in each mesh differ by a factor of approximately three between the coarse and medium grids and approximately two between the medium and fine mesh. The WBNP coarse and fine grids were generated by a global coarsening/refinement of the medium spacing parameters (VGRIDns sourcing terms) of 1 and 0.495, respectively. The minimum wall spacing between the grids differs by a similar factor. The same refinement factor used to generate the WB fine grid could not be used to generate the WBNP fine grid due to limitations of the grid generation software. At the time of the study, VGRIDns could not generate a larger grid due to limitations in the restart capability. This limitation has since been removed. Tables 1 and 2 summarize the global grid sizes for the family of WB and WBNP node-centered grids. Tables 3 and 4 illustrate the effect of coarsening and refinement on the chordwise spacings and viscous spacings. Figure 5 compares the chordwise spacing on the upper wing surface at the crank between the coarse, medium and fine grids. Figure 6 compares the chordwise spacing on the exterior nacelle surface at the inboard 60° station. Both figures show a consistent coarsening and refinement of the chordwise spacing on the wing and nacelle. The wing and nacelle blunt trailing edges were refined explicitly (see Tables 3 and 4). The geometric growth in the boundary layer was modified for the fine grids so that the geometric extent of the advancing layers was approximately the same as for the medium grids (see Tables 3 and 4).

Computational Results

DPW-II had two required and two optional cases for the participants: Case 1 was a transonic cruise condition at a constant lift, Case 2 was a transonic drag polar at the same cruise Mach number, Case 3 was an optional comparison of "tripped" and "fully turbulent" solutions for the constant lift condition, and Case 4 was an optional drag rise prediction at constant lift (see Table 5). All cases were run at the test Reynolds number based on geometric chord Re_c and were assumed to be fully turbulent unless otherwise noted. For tripped cases, the wing boundary layer transition was specified on the lower surface at 25% of chord and on the upper surface at 5% of chord at the root, 15% at the crank, 15% at $\eta = 0.844$, and 5% at the tip. (Note that for the NSU3D Case 3 results, transition is not specified on the lower wing in close proximity to the pylon-wing junction, due to the presence of a shock wave in this region for certain flow conditions. The removal of this transition patch was verified to result in a difference of less than one drag count.) The inner nacelle boundary layer transition was specified at 9.27% of chord (15 mm model scale) from the inlet. The outer nacelle boundary layer transition was specified at 7.41% of chord (12 mm model scale) from the inlet. Results from

Case 1*	$M = 0.75, C_L = 0.500 \pm 0.001$ $Re_c = 3 \times 10^6$, Fully Turbulent WB and WBNP Coarse, Medium and Fine Grids
Case 2*	$M = 0.75$ $\alpha = -3°, -2°, -1°, 0°, 1°, 2°$ $Re_c = 3 \times 10^6$, Specified Transition (or Fully Turbulent if necessary) WB and WBNP Medium Grids
Case 3	$M = 0.75, C_L = 0.500 \pm 0.001$ $Re_c = 3 \times 10^6$, Specified Transition WB and WBNP Medium Grids
Case 4	$C_L = 0.500 \pm 0.001$ $M = 0.50, 0.60, 0.70, 0.72, 0.74,$ $0.75, 0.76, 0.77$ $Re_c = 3 \times 10^6$, Specified Transition WB and WBNP Medium Grids

* Required

Table 5   Required and optional cases for the DPW-II.

Code	Eq.	Diff. Scheme	Turb. Model
USM3D	FNS	Roe	SA+WF
NSU3D	TL3D	CD/MD	SA
FUN3D	FNS	Roe	SA

Table 6   Baseline code configurations.

USM3D, NSU3D and FUN3D solutions for the required Cases 1 and 2 were submitted to the workshop and are included in the current paper. Results from NSU3D and FUN3D solutions for the optional Case 3 were also submitted to the workshop and are included in the current paper. NSU3D results for the optional Case 4 were submitted to the workshop but not included in the current paper. For clarity, the discussion of Case 3 results will follow Case 1 discussions.

The USM3D results were computed on the cell-centered grids and, the FUN3D and USM3D results were computed on the node-centered grids. For each of the codes, a "best" or "standard" practices method for executing the calculations was chosen. The configuration of each code is compared in Table 6 and is referred to as the baseline code configuration. TL3D refers to a thin-layer approximation in all directions, and FNS refers to full Navier-Stokes. CD refers to a central difference scheme with matrix dissipation (MD).

All code solutions were iterated until the residual of the flow equations and turbulence model equation were reduced by several orders of magnitude, and the forces and moments were asymptotically converged to the accu-

racy prescribed by the workshop. For total lift the accuracy was 0.001, for total drag the accuracy was 0.00001, and for the pitching moment the accuracy was 0.0001. For several Case 2 solutions with significant flow separation, the forces and moments did not converge asymptotically. These are noted in the results section. For the medium grid, the USM3D Case 1 WB solution converged in 2500 iterations which took 5.6 GBytes of total memory and 5.9 hours on 48 Origin 3000 (400 MHz) processors. For the medium grid, the FUN3D Case 1 WB solution converged in 2600 iterations which took 9 GBytes of total memory and 17 hours on 24 Pentium 4 (2.66 GHz) processors. For the medium grid, the NSU3D Case 1 WB solution converged in 500 multigrid cycles which took 5.5 GBytes of total memory and 5 hours on 16 Pentium (1.7 GHz) processors. NSU3D took significantly less CPU time to converge to the prescribed accuracy possibly due to the use of thin-layer approximations and multi-grid acceleration.

Case 1 – Constant Lift Condition

WB Forces and Moments

The $M = 0.75$, $C_L = 0.500$ case was computed on the WB coarse, medium and fine grids for all codes in their baseline configuration. Figures 7, 8, 9, and 10 show the WB angle of attack, total drag, pressure drag, viscous drag and pitching moment versus $N^{-2/3}$, where N is the number of cells for the cell-centered code and the number of nodes for the node-centered codes. (In the asymptotic range, one would expect a linear variation in forces or moments with $N^{-2/3}$ for a second order scheme.) Thus, results using finer grids appear to the left in the figures, and results using coarser grids appear to the right. The experimental values are included in Figs. 7 - 10 for reference. Table 7 shows a summary of all WB Case 1 (and Case 3) calculations along with the experimental data for reference.

Figs. 7 - 10 show that the angle of attack, forces and moments computed with FUN3D and NSU3D vary monotonically with grid refinement although the three data points do not fall on a straight line. For the USM3D results, the angle of attack and pitching moment do not vary monotonically with grid refinement although the drag forces do vary monotonically (see also Table 7). The dashed lines in Fig. 8 show a Richardson's extrapolation of total drag based on the medium and fine grids which were computed assuming a second order convergence rate for each code. Based on this extrapolation, the infinite-grid total drag is 273, 278 and 274 counts for USM3D, FUN3D and NSU3D, respectively. For the total drag force the observed order of convergence[23] was 2.8, 3.4 and 1.9 for USM3D, FUN3D and NSU3D, respectively. Using the observed convergence rate, the infinite-grid total drag is 274, 280 and 274 counts for for
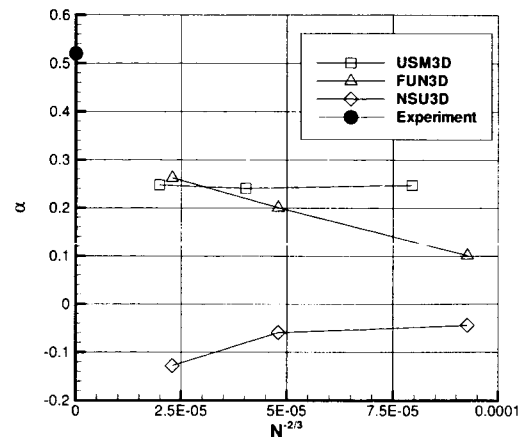

Fig. 7   Comparison of WB angle of attack versus number of cells or vertexes to the -2/3 power at $M = 0.75$, $C_L = 0.500$.
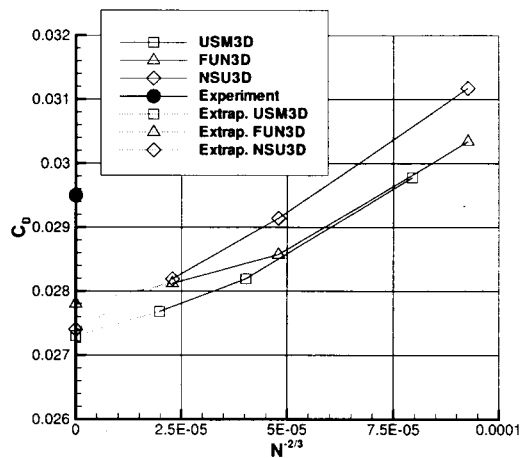

Fig. 8   Comparison of WB total drag versus number of cells or vertexes to the -2/3 power at $M = 0.75$, $C_L = 0.500$.

USM3D, FUN3D and NSU3D, respectively.

While the code-to-code variation in total drag decreases with grid refinement, the variation in angle of attack and pitching moment is increasing. Figures 7 and 10 shows that the USM3D and FUN3D predicted angle of attack and pitching moment at constant lift is increasing with grid refinement which improves the correlation with experiment. The NSU3D angle of attack is becoming increasingly negative which degrades the correlation with the experiment. The total drag range decreased with grid refinement from 14 counts on the coarse grid to 9 counts on the medium grid to 5 counts on the fine grid. The range in infinite-grid total drag between the three codes

Code	Mesh	Specified Transition	α	C_L	C_D	C_{Dp}	C_{Dv}	C_M
Exp.	—	Yes	0.52	0.500	0.0295	—	—	-0.1211
USM3D	Coarse	No	0.248	0.501	0.02978	0.01794	0.01184	-0.1289
USM3D	Medium	No	0.241	0.500	0.02819	0.01624	0.01195	-0.1307
USM3D	Fine	No	0.248	0.499	0.02768	0.01547	0.01221	-0.1308
FUN3D	Coarse	No	0.102	0.500	0.03034	0.01812	0.01221	-0.1309
FUN3D	Medium	No	0.201	0.500	0.02857	0.01646	0.01210	-0.1269
FUN3D	Fine	No	0.263	0.500	0.02812	0.01600	0.01212	-0.1254
FUN3D	Medium	Yes	0.059	0.500	0.02747	0.01586	0.01161	-0.1331
NSU3D	Coarse	No	-0.044	0.500	0.03117	0.01804	0.01313	-0.1444
NSU3D	Medium	No	-0.059	0.500	0.02914	0.01608	0.01306	-0.1485
NSU3D	Fine	No	-0.128	0.499	0.02819	0.01524	0.01294	-0.1518
NSU3D	Medium	Yes	-0.172	0.500	0.02795	0.01555	0.01240	-0.1554

Table 7   Summary of WB $M = 0.75$, $C_L = 0.500$ results.
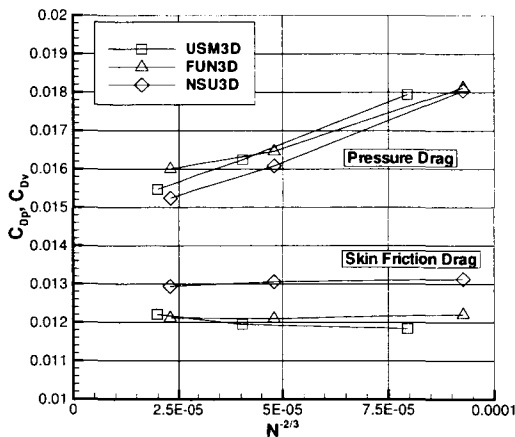
Fig. 9   Comparison of WB pressure and viscous drag versus number of cells or vertexes to the -2/3 power at $M = 0.75$, $C_L = 0.500$.

Fig. 10   Comparison of WB pitching moment versus number of cells or vertexes to the -2/3 power at $M = 0.75$, $C_L = 0.500$.

is also 5 counts. For the collective of workshop solutions, the range for the WB on the medium grids was 48 counts and the average moving range was 8 counts.[10] The estimated code-to-code population standard deviations of total drag for the nested solutions was ±7.3 counts for the WB.[10] (Note the estimated code-to-code WB population standard deviation from the workshop did not show any consistent decrease with grid refinement. The stated value of standard deviation is an average for the coarse, medium and fine grids.) For USM3D, FUN3D and NSU3D, the grid refinement degrades the correlation with the experimental total drag. For FUN3D, the infinite-grid total drag is 15 counts below the experimental value. For USM3D and NSU3D the infinite-grid total drag is 21 counts below the experimental value. This un-
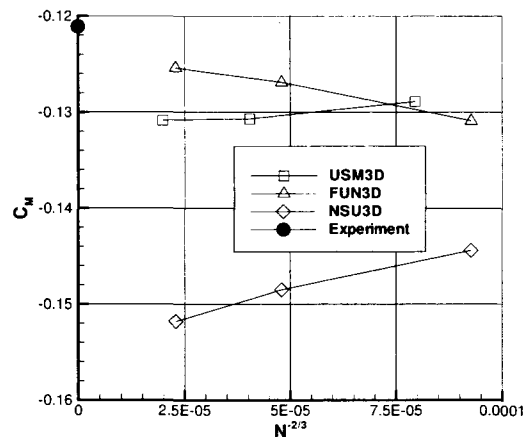
der prediction of drag with grid refinement is consistent with the workshop sample medians presented in Ref. 10.

The pressure drag and viscous drag components did not show a consistent decrease in range with grid refinement (see Fig. 9). The pressure drag range increased with grid refinement from 2 counts on the coarse grid to 4 counts on the medium grid to 8 counts on the fine grid. At the same time, the viscous drag range decreased with grid refinement from 13 counts on the coarse grid to 10 counts on the medium grid to 8 counts on the fine grid.

WB Surface Pressures

Figures 11, 12 and 13 show the grid convergence of the wing chordwise surface pressure distributions for the USM3D, FUN3D and NSU3D solutions, respectively.

12

The computational results are shown at seven of the eight experimental span locations along with the experimental pressure coefficients for reference. Although both the WB and WBNP configurations are shown, the current discussion will focus on the WB configuration. These pressure distributions indicate two of the relevant flow features at this lift condition: a separation bubble near the trailing edge of the upper wing-root juncture and a mild normal shock across the span of the upper wing near the quarter chord. (A comparison of surface restricted streamlines shown later in the paper indicates that differences in the inboard $\eta = 0.150$ pressure distributions are indicative of differences in the wing-root juncture separation.)

A comparison of chordwise pressure distributions for the USM3D solutions in Fig. 11 shows that the pressures changed very little with grid refinement. The small variation in the pressure distributions is consistent with the small variation in angle of attack and pitching moment with grid refinement shown in Figs. 7 and 10. However, the variation in total drag and pressure drag with grid refinement shown in Figs. 8 and 9 is significant. The chordwise pressure distributions predicted by USM3D compare well with the experimental values on the inboard span of the wing. Through the mid-span of the wing the predicted shock is forward of the experimental data, and at the tip the predicted shock is much weaker and forward of the experimental data.

A comparison of chordwise pressure distributions for the FUN3D solutions in Fig. 12 indicates that the area of wing-root juncture separation increased with grid refinement as the spanwise shock strengthened and moved aft. The increased inboard separation is consistent with the increase in angle of attack required for constant lift shown in Fig. 7. Similarly the variation in shock strength and location is consistent with the increase in pitching moment shown in Fig. 10. An increase in drag would be expected to correspond with the increase in angle of attack required to maintain the constant lift condition. However, the drag variation shown in Fig. 8 decreased with grid refinement which would indicate that the effect of grid refinement was more significant than the effect of increasing angle of attack. Figure 12 shows that grid refinement improves the comparison of predicted chordwise pressure distribution with the experimental values on the inboard span of the wing. Through the mid-span of the wing, the predicted shock is forward of the experimental data, and at the tip the predicted shock is much weaker and forward of the experimental data. Grid refinement slightly improves the comparison of predicted shock location across the span of the wing.

A comparison of chordwise pressure distributions for the NSU3D solutions in Fig. 13 shows that the flowfield in the area of wing-root juncture separation changed very little with grid refinement while the spanwise shock slightly strengthened and moved forward. The shift in shock location and strength is consistent with the decrease in angle of attack, drag and pitching moment with grid refinement shown in Figs. 7 - 10. At $\eta = 0.150$, the NSU3D solutions predicted greater suction on the upper wing surface than the experimental data which indicate a smaller wing-root juncture separation than measured in the experiment. Through the mid-span of the wing the predicted shock is forward of the experimental data, and at the tip the predicted shock is much weaker and forward of the experimental data. Grid refinement slightly degrades the comparison of predicted shock location across the span of the wing.

A code-to-code comparison of chordwise pressure distributions for the WB fine mesh solutions is shown in Fig. 14. The USM3D and FUN3D results are very similar across the span of the wing. This is consistent with the close correlation of the USM3D and FUN3D fine grid results shown in Figs. 7 and 10. The NSU3D solution predicted a smaller wing-root juncture separation than the other two codes and also a weaker shock across the span of the wing. This is consistent with the lower angle of attack and pitching moment predicted by NSU3D in comparison with USM3D and FUN3D results shown in Figs. 7 and 10. None of the predicted outboard pressure distributions matched the experimental data very well. Several participants at the workshop noted that the correlation of the computed WB surface pressures with the experiment were greatly improved by matching the experimental angle of attack.[8]

WBNP Forces and Moments

The $M = 0.75$, $C_L = 0.500$ case was computed on the WBNP coarse, medium and fine grids for all codes in their baseline configuration. Figures 15, 16, 17, and 18 show the WBNP angle of attack, total drag, pressure drag, viscous drag and pitching moment versus $N^{-2/3}$. Additionally, the incremental drag due to the engine installation ΔC_D is shown in Fig. 19. In Fig. 19, the drag increment is plotted versus a characteristic grid spacing Δh^2 due to the fact that the comparable WB and WBNP grids have a different number of unknowns. (Recall that the node-centered WB and WBNP fine grids were not generated with the same global refinement factor. The incremental drag results from the fine node-centered grid solutions are plotted at the coarser relative WBNP spacing.) The experimental values are included in Figures 15 - 19 for reference. Table 8 shows a summary of all WBNP Case 1 (and Case 3) calculations along with the experimental data for reference.

Figs. 15 - 18 show that the angle of attack, forces and moments computed with USM3D vary monotonically with grid refinement and the three data points do appear
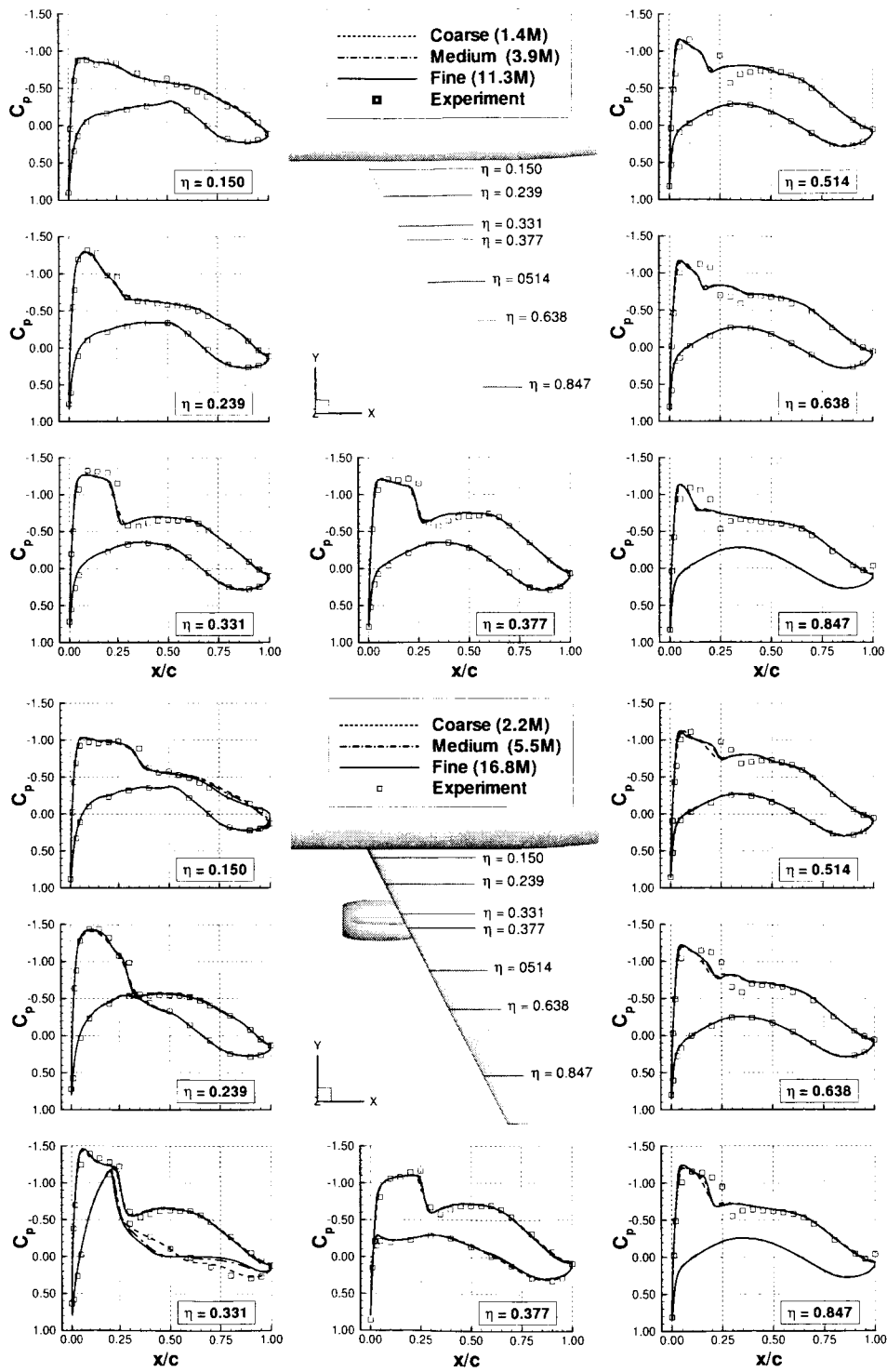
Fig. 11 Grid convergence of wing surface pressure distributions predicted by USM3D at $M = 0.75$, $C_L = 0.500$.
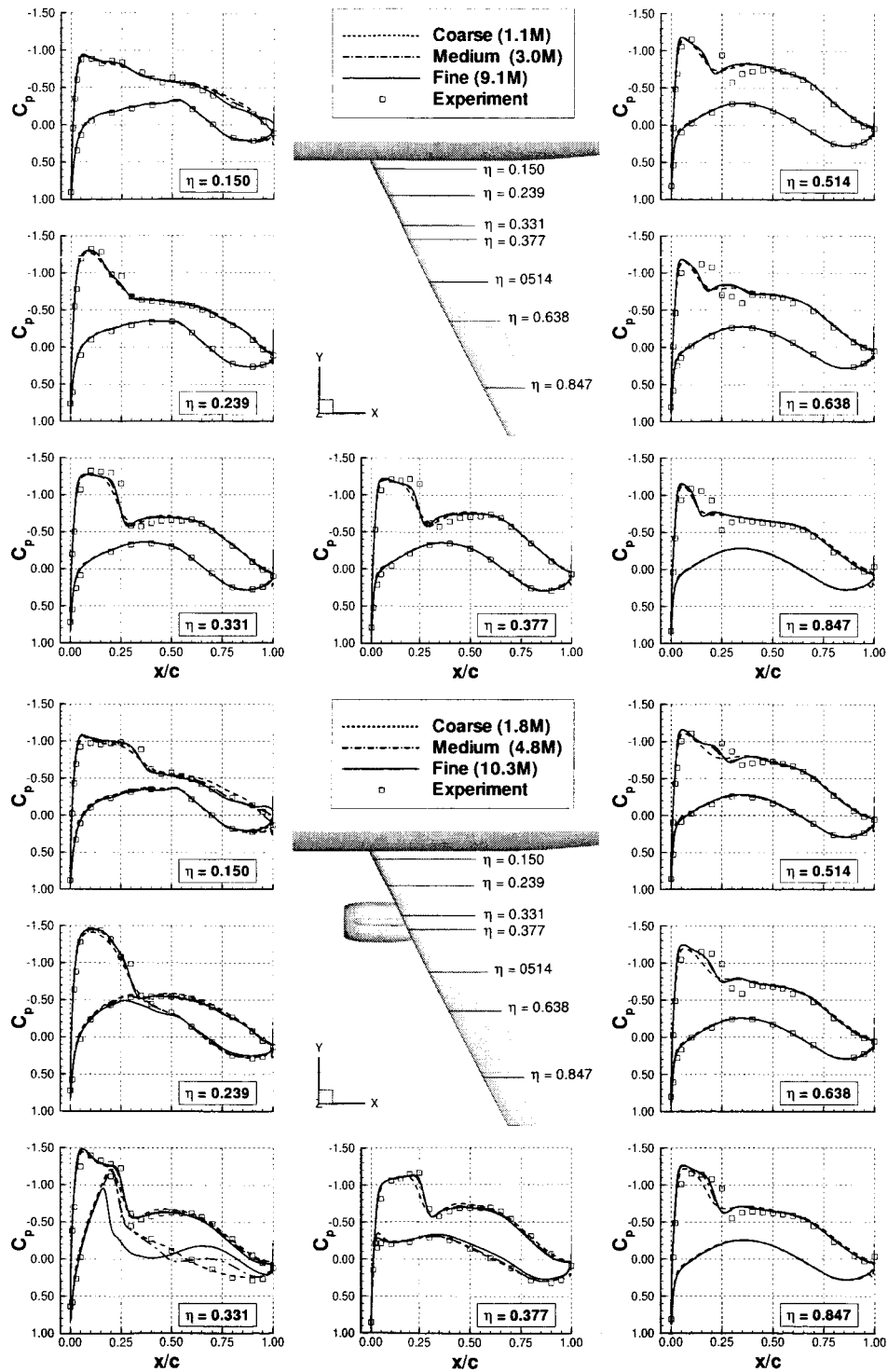
Fig. 12   Grid convergence of wing surface pressure distributions predicted by FUN3D at $M = 0.75$, $C_L = 0.500$.
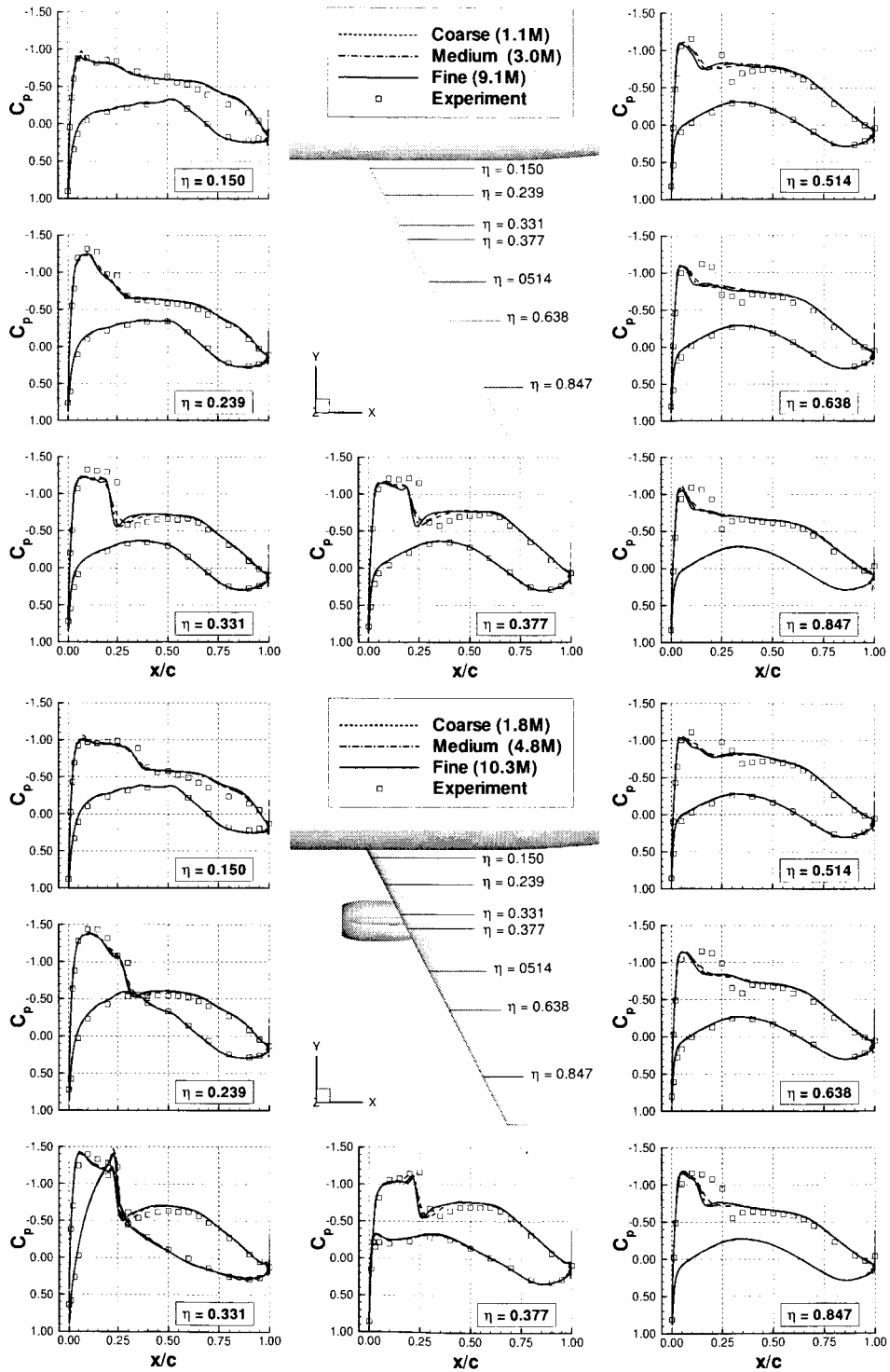
Fig. 13   Grid convergence of wing surface pressure distributions predicted by NSU3D at $M = 0.75$, $C_L = 0.500$.
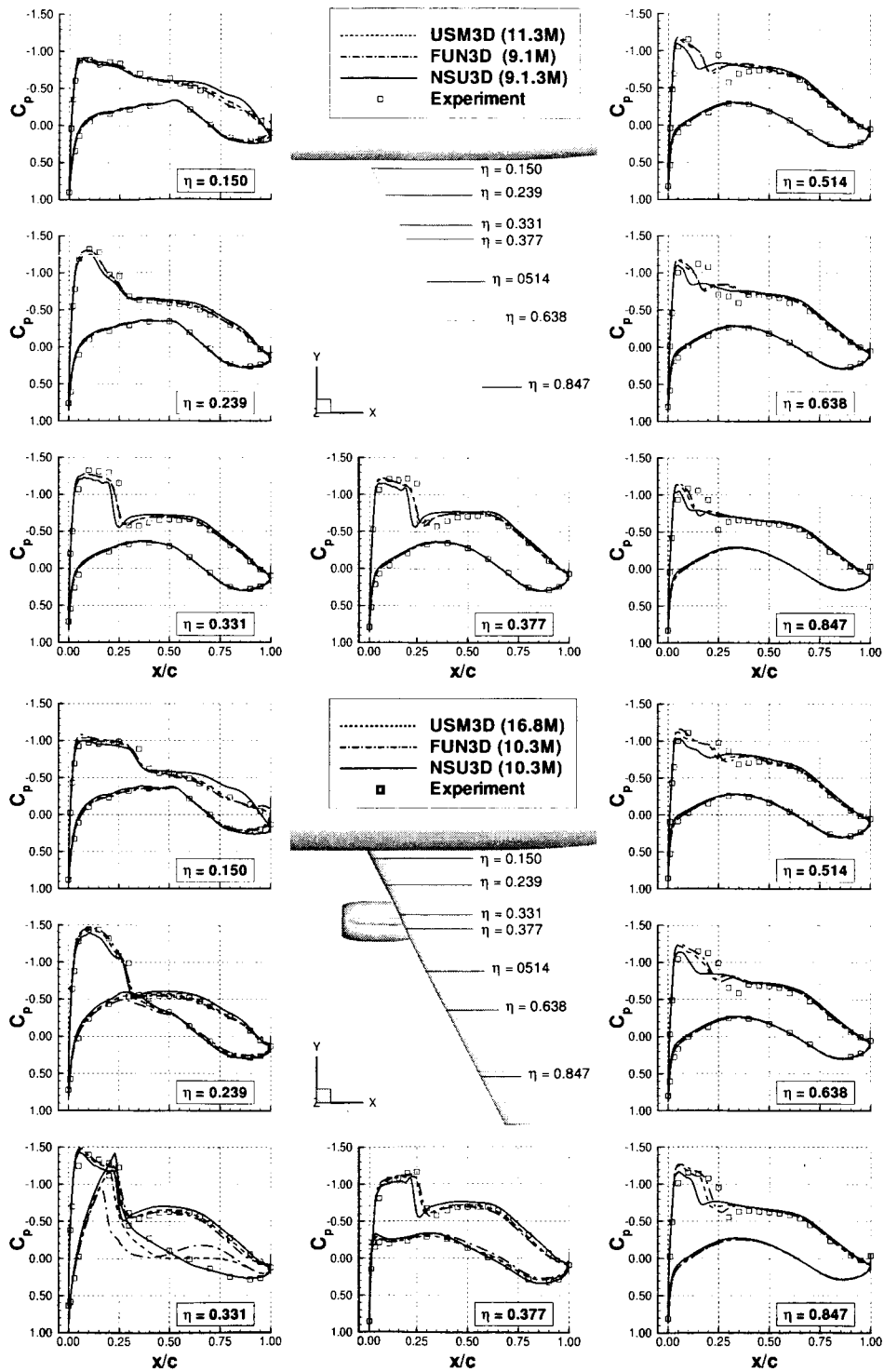
Fig. 14   Comparison of fine grid wing surface pressure distributions at $M = 0.75$, $C_L = 0.500$.

Code	Mesh	Specified Transition	α	C_L	C_D	C_{Dp}	C_{Dv}	C_M	ΔC_D
Exp.	—	Yes	1.00	0.500	0.0338	—	—	-0.1199	0.0043
USM3D	Coarse	No	0.729	0.501	0.03388	0.01984	0.01404	-0.1292	0.00410
USM3D	Medium	No	0.805	0.500	0.03235	0.01821	0.01414	-0.1275	0.00416
USM3D	Fine	No	0.849	0.500	0.03167	0.01725	0.01442	-0.1262	0.00399
FUN3D	Coarse	No	0.679	0.500	0.03524	0.02092	0.01432	-0.1280	0.00490
FUN3D	Medium	No	0.945	0.500	0.03341	0.01918	0.01423	-0.1165	0.00484
FUN3D	Fine	No	1.015	0.500	0.03357	0.01933	0.01424	-0.1120	0.00545
FUN3D	Medium	Yes	0.860	0.500	0.03305	0.01939	0.01366	-0.1179	0.00558
NSU3D	Coarse	No	0.462	0.500	0.03637	0.02078	0.01559	-0.1461	0.00520
NSU3D	Medium	No	0.466	0.500	0.03370	0.01819	0.01552	-0.1477	0.00456
NSU3D	Fine	No	0.381	0.500	0.03278	0.01737	0.01541	-0.1539	0.00459
NSU3D	Medium	Yes	0.349	0.500	0.03259	0.01789	0.01469	-0.1554	0.00464

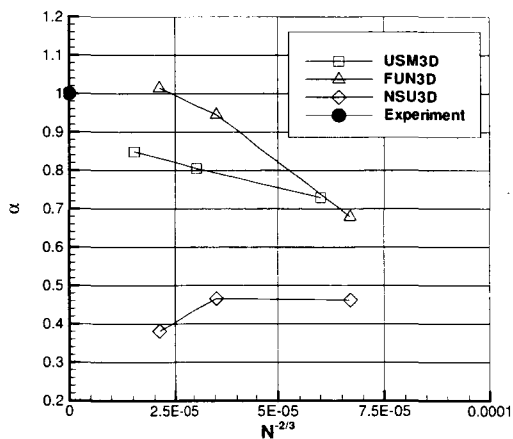Table 8 Summary of WBNP $M = 0.75$, $C_L = 0.500$ results.

Fig. 15 Comparison of WBNP angle of attack versus number of cells or vertexes to the -2/3 power at $M = 0.75$, $C_L = 0.500$.

Fig. 16 Comparison of WBNP total drag versus number of cells or vertexes to the -2/3 power at $M = 0.75$, $C_L = 0.500$.

to be very close to a straight line. For the FUN3D results, the angle of attack and pitching moment vary monotonically with grid refinement although not on a straight line. The FUN3D drag forces do not vary monotonically with grid refinement. For the NSU3D results, the drag and pitching moment vary monotonically with grid refinement although also not on a straight line, but the angle of attack does not vary monotonically. The dashed lines in Fig. 16 show a Richardson's extrapolation of total drag based on the medium and fine grids which were computed assuming a second order convergence rate for each code. Based on this extrapolation, the infinite-grid total drag is 311, 338 and 317 counts for USM3D, FUN3D and NSU3D results, respectively.
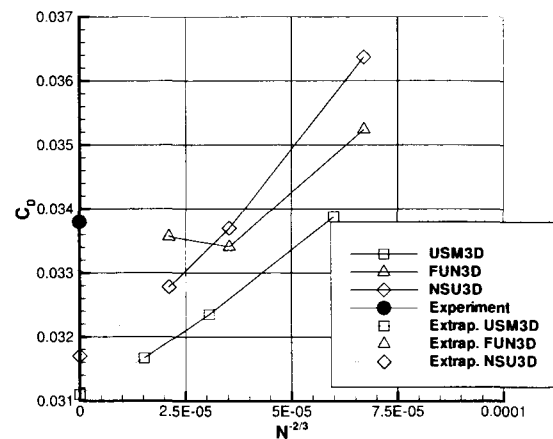
Figs. 15 and 18 show that the code-to-code variation

in angle of attack and pitching moment is increasing. The USM3D and FUN3D predicted angle of attack and pitching moment at constant lift is increasing with grid refinement which improves the correlation with the experimental data. However, the NSU3D angle of attack is becoming increasingly negative which degrades the correlation with the experiment.

The code-to-code variation in total drag does not vary monotonically with grid refinement as shown in Fig. 16. The total drag range decreased with grid refinement from 25 counts on the coarse grid to 13 counts on the medium grid but increased to 19 counts on the fine grid. The range of infinite-grid total drag between the three codes is 27 counts. The estimated code-to-code population standard deviations of total drag for the nested solutions
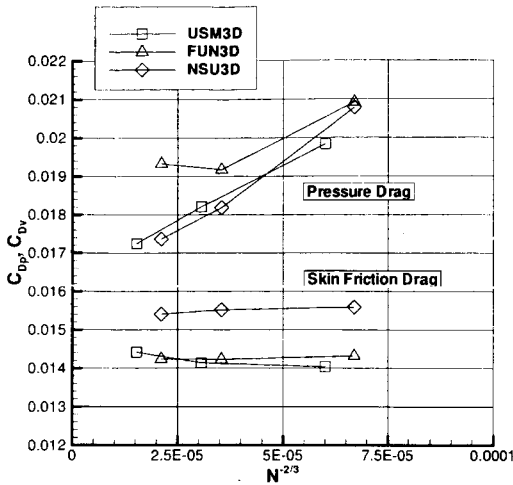
18

Fig. 17 Comparison of WBNP pressure and viscous drag versus number of cells or vertexes to the -2/3 power at $M = 0.75$, $C_L = 0.500$.
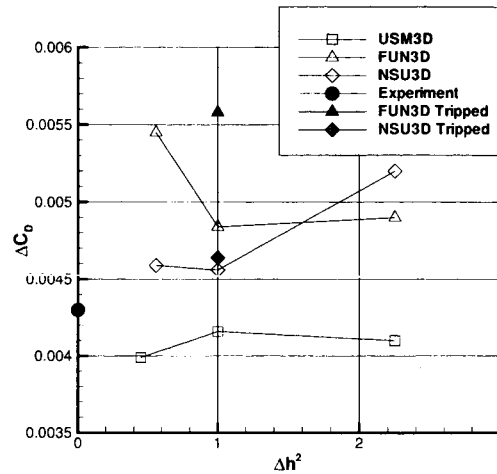

Fig. 19 Comparison of drag increment versus characteristic grid spacings to the 2 power at $M = 0.75$, $C_L = 0.500$.
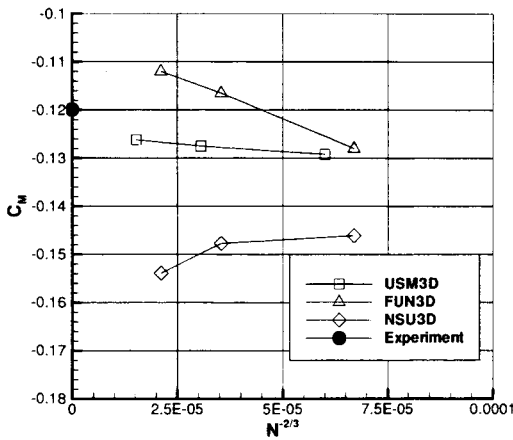

Fig. 18 Comparison of WBNP pitching moment versus number of cells or vertexes to the -2/3 power at $M = 0.75$, $C_L = 0.500$.

proves the correlation with experiment, and the infinite-grid estimate actually matches the experiment. However, a comparison of wing pressure distributions and surface restricted streamlines for the FUN3D fine grid WBNP shown later in the paper indicates that the computation does not predict the same flow features which were observed in the experiment.

The pressure drag also did not show a consistent decrease in range with grid refinement although the viscous drag did (See Fig. 17). The pressure drag range decreased with grid refinement from 11 counts on the coarse grid to 10 counts on the medium grid but increased to 20 counts on the fine grid. The viscous drag range decreased with grid refinement from 16 count on the coarse grid to 14 counts on the medium grid to 12 counts on the fine grid.

The code-to-code variation in incremental drag did not vary monotonically with grid refinement as shown in Fig. 19. The incremental drag range decreased with grid refinement from 11 counts on the coarse grid to 6 counts on the medium grid but increased to 15 counts on the fine grid. The estimated code-to-code population standard deviations of incremental drag for the nested solutions was ±8 counts for the engine increment.[10] The USM3D and NSU3D medium and fine grid incremental drag values are within 3 counts of the experimental value, but the USM3D results tend to be low and the NSU3D results tend to be high. The FUN3D fine grid incremental drag value is 12 counts higher that the experiment. The workshop sample medians for the incremental drag show a decrease in incremental drag with grid refinement, and the fine grid sample median is 7 counts higher than the experiment.[10]

was ±11.4 counts for the WBNP.[10] (Note the estimated code-to-code WBNP population standard deviation from the workshop did not show any consistent decrease with grid refinement. The stated value of standard deviation is an average for the coarse, medium and fine grids.)

For USM3D and NSU3D, the grid refinement decreases the total drag and degrades the correlation with the experimentally measured total drag. This decrease in drag with grid refinement is consistent with the workshop sample medians presented in Ref. 10 although the workshop sample median for the fine grid solutions matches the experimental drag. For FUN3D, grid refinement im-

19

WBNP Surface Pressures

Figures 11 - 13 compare the grid convergence of the wing surface pressure distributions for the WB and WBNP solutions. The WBNP pressure distributions indicate that the wing-root junction separation predicted for the WB was still present with the engine installation. Also the normal shock was still evident across the span of the upper-wing near the quarter chord. The lower surface pressure distribution near the nacelle/pylon show an influence due to the engine. Additionally, Figs. 20 and 21 show the grid convergence of the nacelle chordwise surface pressures at three experimental span locations for the USM3D and FUN3D solutions, respectively. The experimental pressure coefficients are also included for reference.

The WBNP chordwise pressure distributions for the USM3D solutions shown in Fig. 11 do not vary significantly with grid refinement except in the area near the inboard pylon. The correlation of the WBNP pressure distributions with the experimental data is very similar to the WB correlation. The pressure distributions predicted by USM3D compare well with the experimental values on the inboard span of the wing. Through the mid-span of the wing the predicted shock is forward of the experimental data, and at the tip the predicted shock is much weaker and forward of the experimental data. In the area of the inboard pylon $\eta = 0.331$, grid refinement degrades the correlation with the experiment. The fine grid solution predicts more separation near the inboard wing-pylon juncture than seen in the experiment. Figure 20 shows very small variations in the USM3D nacelle surface pressures with grid refinement. The correlation with the experiment is very good with some over prediction of the suction for the inboard $\theta = 300°$ nacelle station.

Figure 12 shows that the effect of grid refinement for the FUN3D WBNP solutions is similar that shown for the WB solutions in terms of the variation of wing-root juncture separation and normal shock strength/location. The correlation of the FUN3D WBNP pressure distributions with the experimental data is also very similar to the WB correlation in the areas of the wing-root juncture separation and normal shock. In the area of the inboard pylon $\eta = 0.331$, the lower-wing surface pressure distribution varies significantly with grid refinement which degrades the correlation with the experiment. The fine grid solution predicts much more separation near the inboard wing-pylon juncture than seen in the experiment. Figure 20 shows very small variations in the FUN3D nacelle surface pressures with grid refinement except in the area of the inboard $\theta = 300°$ nacelle station. The correlation with the experiment is very good except for the under prediction of the suction for the fine grid inboard $\theta = 300°$ nacelle station.

Figure 13 shows that the effect of grid refinement for the NSU3D WBNP solutions is similar that shown for the WB solutions in terms of the variation of wing-root juncture separation and normal shock strength/location. The correlation of the NSU3D WBNP pressure distributions with the experimental data is also very similar to the WB correlation in the areas of the wing-root juncture separation and normal shock. In the area of the inboard pylon $\eta = 0.331$, the lower surface pressure distribution does not vary significantly with grid refinement, and the correlation with the experiment is very good in this area.

A code-to-code comparison of chordwise pressure distributions for the WBNP fine mesh solutions is shown in Fig. 14. Figure 14 shows that the code-to-code variation for the WBNP solutions is similar to the code-to-code variation for the WB solutions in terms of the variation of wing-root juncture separation and normal shock strength/location. The most significant code-to-code variation in pressures is in the area of the inboard wing-pylon juncture separation. None of the predicted outboard pressure distributions matched the experimental data very well. Several participants at the workshop noted that the correlation of the computed WBNP surface pressures with the experiment were greatly improved by matching the experimental angle of attack.[8]

WBNP Surface Restricted Streamlines

Figure 22 shows an upper planform view of the DLR-F6 wind-tunnel model with oil flow patterns at the cruise lift condition. Note the nacelle installation is different in Fig. 22 that the one used for the workshop calculations, but the qualitative flow feature will be similar. The oil flow patterns show the wing-root juncture separation as well as a trailing-edge separation pattern from the wing crank to near the tip. Figures 23, 24 and 25 show the surface restricted streamlines for the USM3D, FUN3D and NSU3D fine grid WBNP solutions, respectively. In comparison with the experiment, the USM3D and FUN3D results show a similarly-sized wing-root juncture flow separation and a similarly-sized wing trailing edge separation. However, the NSU3D results predict a much smaller wing-root juncture flow separation and a smaller wing trailing edge separation. Recall that the code-to-code comparison of wing surface pressures shown in Fig. 14 also indicated a smaller wing-root juncture separation for NSU3D. It is interesting to note that qualitatively, the USM3D and FUN3D upper wing flow patterns are most similar although the total drag predictions for USM3D and NSU3D are closer for the fine grid WBNP solutions. This is probably due to fact that the FUN3D fine grid WBNP solution predicts a much larger inboard pylon separation pattern than USM3D and NSU3D which leads to the much higher drag predictions for FUN3D.
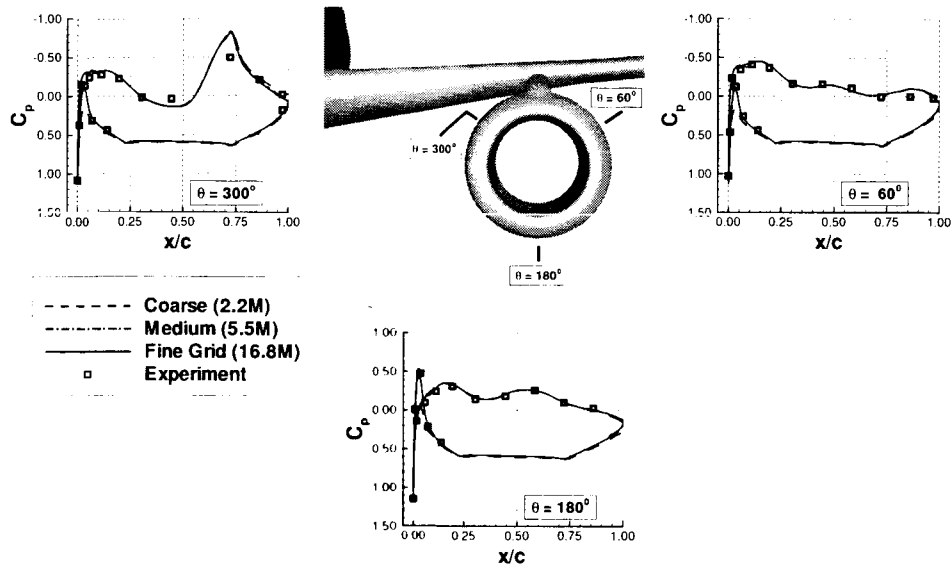
20

Fig. 20 Grid convergence of nacelle surface pressure distributions predicted by USM3D at $M = 0.75$, $C_L = 0.500$.
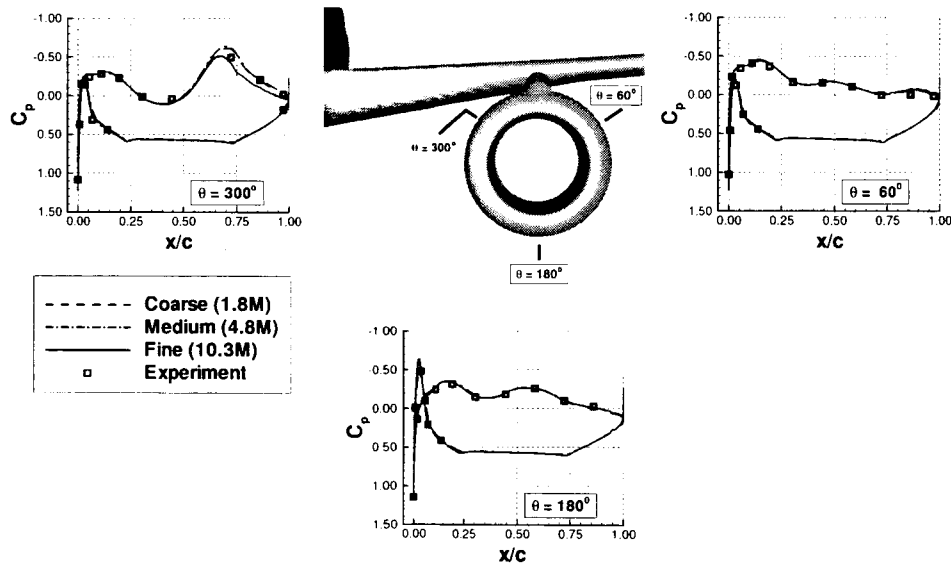

Fig. 21 Grid convergence of nacelle surface pressure distributions predicted by FUN3D at $M = 0.75$, $C_L = 0.500$.
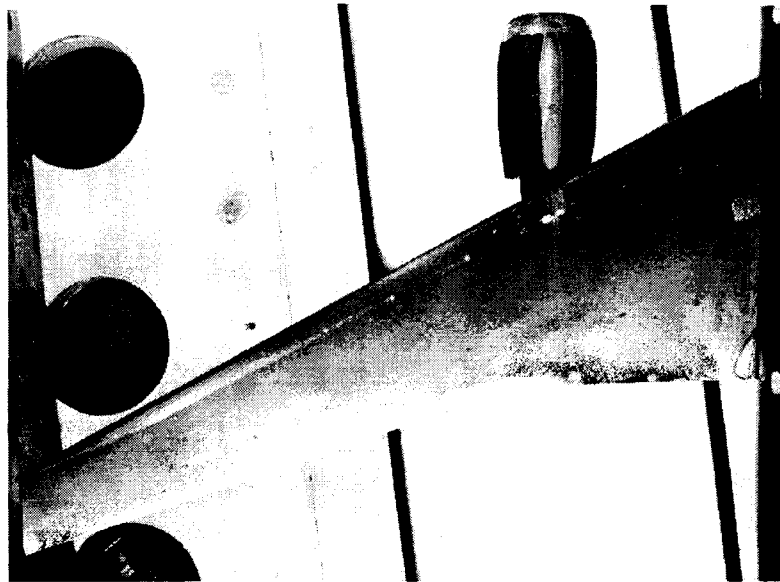
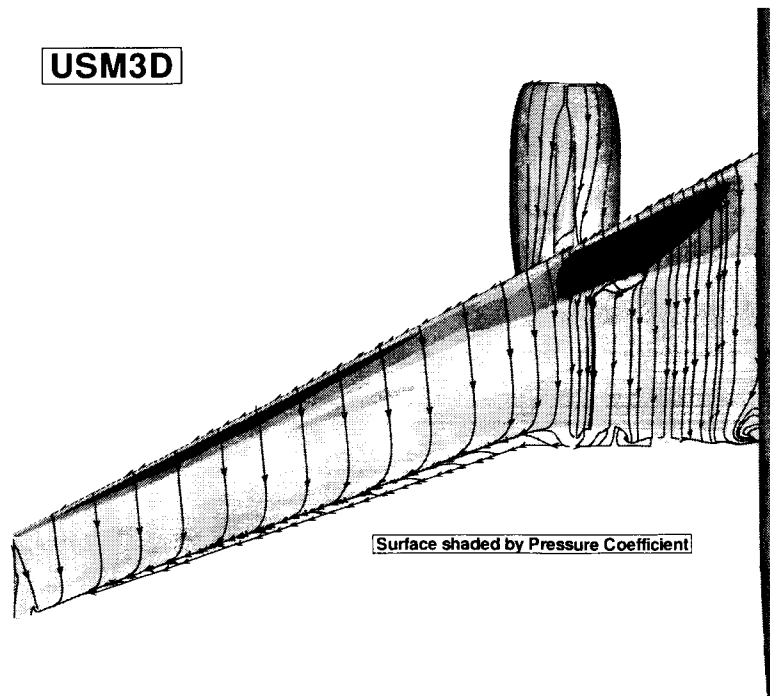**Fig. 22 Experimental oil flow at $M = 0.75$, $C_L = 0.500$. (Note different nacelle configuration)**

Fig. 23 Surface restricted streamlines for fine grid USM3D results at $M = 0.75$, $C_L = 0.500$.
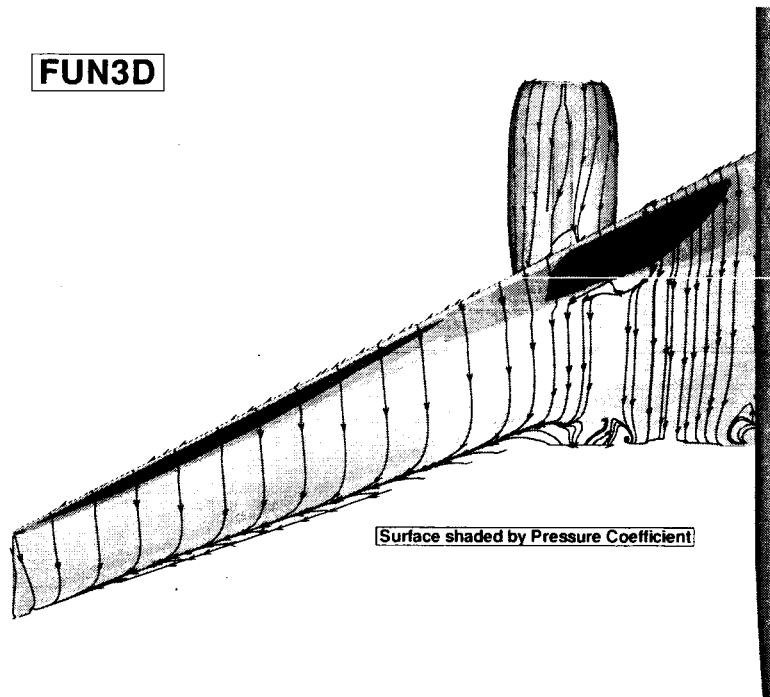
FUN3D

Surface shaded by Pressure Coefficient

Fig. 24 Surface restricted streamlines for fine grid FUN3D results at $M = 0.75, C_L = 0.500$.

NSU3D

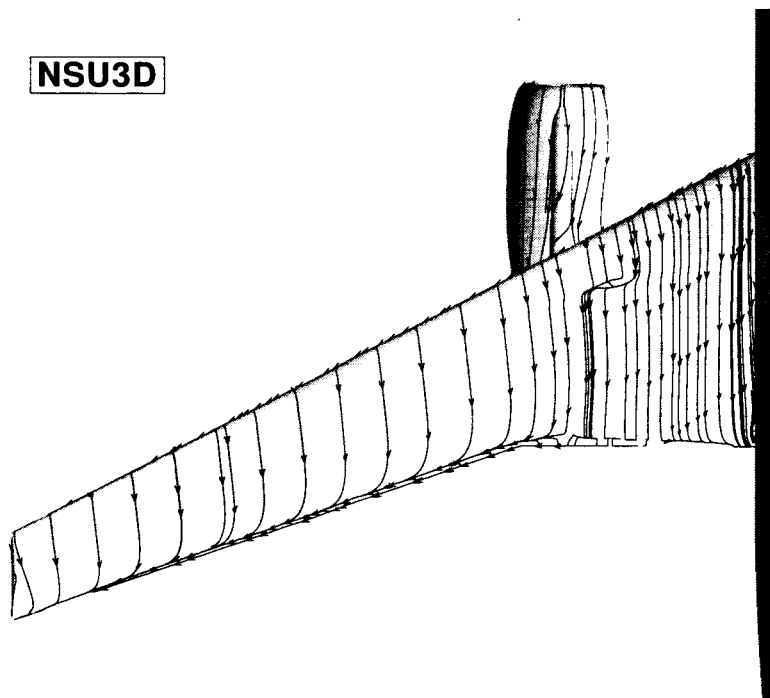Fig. 25 Surface restricted streamlines for fine grid NSU3D results at $M = 0.75, C_L = 0.500$.

Case 3 – Effect of Specified Transition

Case 3 was computed on the WB and WBNP medium grids for FUN3D and NSU3D in their baseline configuration. Table 7 compares the WB forces, moments and angles of attack for tripped flow versus fully turbulent flow. The effect of specifying transition for both codes was to reduce the WB total drag by 11 counts. For both codes, the correlation with the experimental WB forces, moments and angle of attack was not improved by specifying the transition. Table 8 compares the WBNP forces, moments and angles of attack for tripped flow versus fully turbulent flow. The effect of specifying transition for FUN3D was to reduce the WBNP total drag by only 3 counts. The effect of specifying transition for NSU3D was to reduce the WBNP total drag by 11 counts. For both codes, the correlation with the experimental WBNP forces, moments and angle of attack was not improved by specifying the transition. Table 8 also shows that the NSU3D predicted incremental drag was not significantly effected by transition, but the FUN3D predicted incremental drag was increased by ≈ 8 counts (see also Fig. 19) which significantly degraded the correlation with experiment.

Case 2 – Drag Polar

Case 2 was computed on the WB medium grids for all codes in their baseline configuration. Figure 26 shows the wing/body lift versus alpha curves, lift versus total drag curves and lift versus pitching moment curves with the experimental results are included for reference. The lift versus alpha curves for USM3D and FUN3D compare very closely with each other over the range of angle of attack with only a slight variation at the highest angle. The lift versus alpha curve for NSU3D is shifted to the left of the results for the other two codes by approximately 0.15°. All codes over-predict the experimental lift levels across the angle of attack range. The code-to-code comparison for the drag polar shows a consistent variation across the range of data with an increased variation only at the highest angle of attack. USM3D and FUN3D tend to under predict the drag in comparison with the experiment except for the USM3D at the highest angle of attack. NSU3D tends to over-predict the drag at the lower angles of attack and under predict at the higher angles in comparison with experiment. The lift versus pitching moment curves show the largest code-to-code variation which increases at the higher angles of attack. None of the codes predict the pitching moment well although USM3D does predict the break.

Case 2 was computed on the WBNP medium grids for all codes in their baseline configuration. Figure 27 shows the lift versus alpha curves, lift versus total drag curves and lift versus pitching moment curves with the experimental results included for reference. The forces and

moments did not completely converge for the $\alpha = -1°$ FUN3D solution and the $\alpha = -2°$ NSU3D solution. This was probably due to the increased amount of separation predicted in the area of the inboard wing-pylon juncture. The variations in forces and moments were small in comparison with the code-to-code variations so the average values are reported in Fig. 27. No NSU3D solution was computed at $\alpha = -3°$. Note also that there are two solutions provided for FUN3D at $\alpha = -1°, -2°$, and $-3°$ angles of attack. The additional solutions were computed with no restarts from any prior solutions at different angles of attack. For the $\alpha = -1°$ and $-2°$ cases, the solutions show a sensitivity to the solution history. These cases have a significant amount of separated flow in the area of the inboard wing-pylon juncture. The $\alpha = -2°$ solution with no restart has a smaller amount of predicted separation and the predicted drag value lies closer to the experimental polar.

Overall the code-to-code variation in WBNP forces and moments is less consistent across the angle of attack range than for the WB results. The WBNP lift versus alpha curves predicted by the different codes compare well with each other over the lower range of angle of attack, but the slopes of the USM3D and FUN3D results decrease in the $\alpha = -1°$ and $1°$ range and there is an increased code-to-code variation in this range. This decrease in slope at the higher angles of attack is not observed for the NSU3D results or for the experimental data. As for the WB polar, all the codes tend to over-predict the experimental lift levels for most of the angle of attack range. The variation in drag is increased at the lower and higher angle of attack. The computational results show a larger deviation from the experimental values at the lower angles of attack where the computed drag is over-predicted. The lift versus pitching moment curves show the largest code-to-code variation. None of the codes predict the pitching moment well although some of the USM3D and FUN3D results lie closer to the experimental data than for the WB configuration.

Summary

The DPW-II wing/body and wing/body/nacelle/pylon results were compared from three unstructured-grid CFD codes USM3D, FUN3D and NSU3D. Calculations at $C_L = 0.500$ were performed on comparable families of unstructured grids (cell-centered and node-centered) to evaluate the variation in angle of attack, forces and moments with grid refinement. The wing/body grid refinement study showed a decrease in code-to-code variation of drag with grid refinement but an increase in variation of angle of attack and pitching moment. Even though the total drag variation was decreasing with grid refinement, a comparison of grid convergence in wing chordwise pressure distributions for the wing/body configuration in-
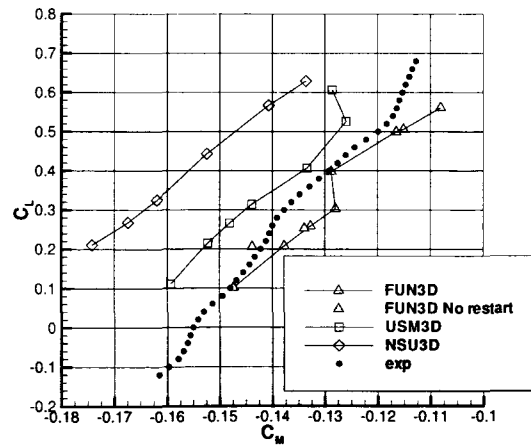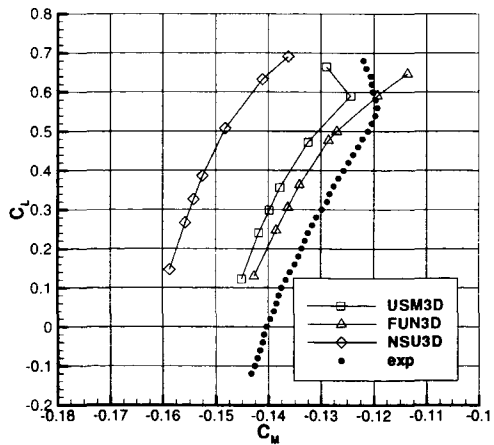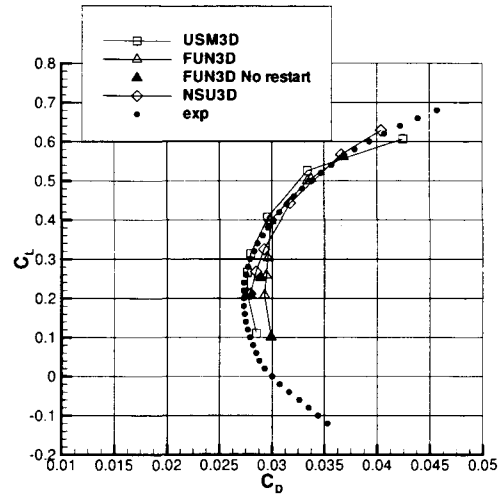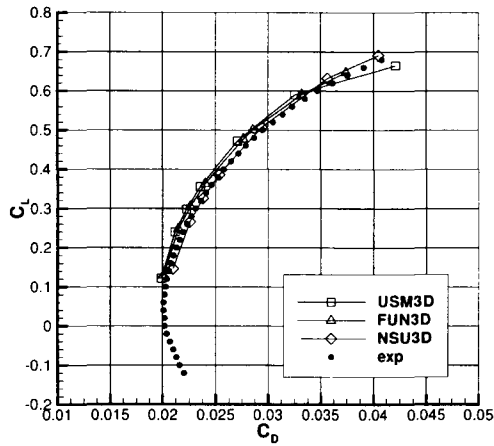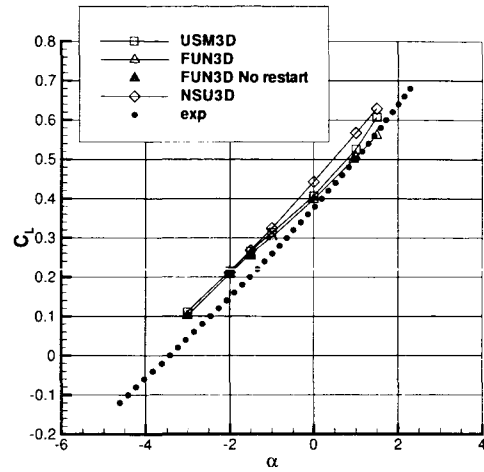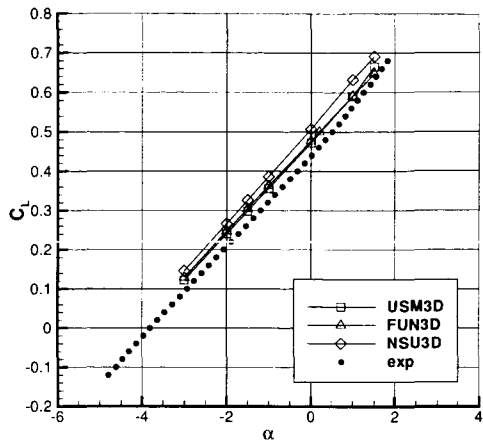
24

Fig. 26 Comparison of force and moment results at $M =$ 0.75 from the WB medium grids.

Fig. 27 Comparison of force and moment results at $M =$ 0.75 from the WBNP medium grids.

25

dicated that some solutions were converged to different shock locations and wing-root juncture flow separation patterns.

The wing/body/nacelle/pylon grid refinement study showed an increase in code-to-code variation of angle of attack, drag, incremental drag and pitching moment with grid refinement. Similar to the wing/body results, a comparison of grid convergence in wing chordwise pressure distributions for the wing/body/nacelle/pylon configuration indicated that some solutions were converged to different shock locations, wing-root juncture flow separation patterns and for this configuration, wing-pylon juncture flow separation patterns.

Overall, grid refinement did not consistently improve the correlation with experimental data for either the wing/body or the wing/body/nacelle pylon configuration. Although the absolute values of total drag predicted by USM3D and NSU3D for the medium and fine grids did not compare well with the experiment, the incremental drag predictions were within ± 3 counts of the experimental data. The correlation with experimental data was not significantly changed by specifying transition for the NSU3D medium grid solutions.

A comparison of medium grid results for the transonic polar indicated a greater code-to-code variation of forces and moments for the wing/body/nacelle/pylon configuration as compared to the wing/body configuration. For the wing/body configuration, all three codes tended to over-predicted the lift and pitching moment in comparison with the experiment but the total drag range spanned the experimental data. For the wing/body/nacelle/pylon configuration, all three codes tended to over-predicted the lift in comparison with the experiment but the total drag range and pitching moment range spanned the experimental data.

Conclusions

Given the effort to create comparable grids, the expectation was to see less code-to-code variation in the forces and moments than was achieved. Although the variation in the constant-lift WB total drag was less than observed for the workshop, the increasing variation in angle-of-attack and pitching moment with grid refinement was surprising. The variation in WBNP total and incremental drag was on the same level as the workshop collective. It is possible that the local resolution of the grids may still be insufficient to capture the relevant flow features especially in the wake region and the area of inboard wing-pylon separation. (Recall the grids have an O-type topology around the trailing edges of the wing and nacelle.) Future analysis with adjoint-based error estimation and adaption may help in identifying the areas of the grid that are not sufficiently resolved for accurate drag prediction.

Qualitatively (surface pressures and separation patterns), the USM3D and FUN3D constant-lift solutions seemed to be more comparable. This could be an effect due to Roe solver vs. artificial dissipation, thin-layer vs. full Navier-Stokes, or fully tetrahedral grids vs. mixed-element grids. Although the thin-layer approximation in NSU3D has been implemented to make the code more efficient, it is unclear whether this is a good compromise for accurate drag prediction. Since many structured grid codes also use the thin-layer approximation, the effect of these approximations is an important area for future research. Investigations into the effects of Roe solver vs. artificial dissipation and fully tetrahedral grids vs. mixed-element grids would also help to quantify their effect on drag prediction for transport configurations. Similarly, a single-code investigation of the effects of using wall-functions vs. integration the turbulence model to the wall would quantify the effects of this approximation on drag prediction. Although the sources of code-to-code variation in force and moment predictions for the three unstructured grid codes have not yet been identified, the current study reinforces the necessity of applying multiple codes to the same application to assess uncertainty.

Acknowledgments

References

[1] Levy, D. W., Zickuhr, T., Vassberg, J., Agrawal, S., Wahls, R. A., Pirzaheh, S., and Hemsch, M. J., "Summary of Data from the First AIAA CFD Drag Prediction Workshop," Tech. Rep. AIAA-2002-0841, Jan. 2002.

[2] Hemsch, M. J., "Statistical Analysis of CFD Solutions from the Drag Prediction Workshop," Tech. Rep. AIAA-2002-0842, Jan. 2002.

[3] Rakowitz, M., Sutcliffe, M., Eisfeld, B., Schwamborn, D. Bleecke, H., and Fassbender, J., "Structured and Unstructured Computations on the DLR-F4 Wing-Body Configuration," Tech. Rep. AIAA-2002-0837, Jan. 2002.

[4] Mavriplis, D. J. and Levy, D. W., "Transonic Drag Prediction Using an Unstructured Multigrid Solver," Tech. Rep. AIAA-2002-0838, Jan. 2002.

[5] Pirzadeh, S. Z. and Frink, N. T., "Assessment of the Unstructured Grid Software TetrUSS for Drag Prediction of the DLR-F4 Configuration," Tech. Rep. AIAA-2002-0839, Jan. 2002.

[6] Vassberg, J., Buning, P. G., and Rumsey, C. L., "Drag Prediction for the DLR-F4 Wing/Body using OVERFLOW and CFL3D on an Overset Mesh," Tech. Rep. AIAA-2002-0840, Jan. 2002.

[7] Lee-Rausch, E. M., Buning, P. B., Mavriplis, D. J., Morrison, J. H., Park, M. A., Rivers, S. M., and Rumsey, C. L., "CFD Sensitivity Analysis of a Drag Prediction Workshop Wing/Body Transport Configuration," Tech. Rep. AIAA-2003-3400, Jun. 2003.

[8] Anon., "2nd AIAA CFD Drag Prediction Workshop, Orlando, FL," //http:aaac.larc.nasa.gov/tsab/cfdlarc/aiaa-dpw, Jun. 2003.

[9]Laflin, K., "Summary of Data from the Second AIAA CFD Drag Prediction Workshop," Tech. Rep. AIAA-2004-0555, Jan. 2004.

[10]Hemsch, M. J. and H., M. J., "Statistical Analysis of CFD Solutions from 2nd Drag Prediction Workshop (Invited)," Tech. Rep. AIAA-2004-0556, Jan. 2004.

[11]Frink, N. T., "Tetrahedral Unstructured Navier-Stokes Method for Turbulent Flows," *AIAA Journal*, Vol. 36, No. 11, Nov. 1998, pp. 1975–1982.

[12]Anderson, W. K., Rausch, R. D., and Bonhaus, D. L., "Implicit/Multigrid Algorithms for Incompressible Turbulent Flows on Unstructured Grids," *Journal of Computational Physics*, Vol. 128, No. 2, 1996, pp. 391–408.

[13]Mavriplis, D. J. and Venkatakrishnan, V., "A Unified Multigrid Solver for the Navier-Stokes Equations on Mixed Element Meshes," *International Journal for Computational Fluid Dynamics*, , No. 8, 1997, pp. 247–263.

[14]Brodersen, O. and Stürmer, "Drag Prediction of Engine-Airframe Interference Effects using Unstructured Navier-Stokes Calculations," Tech. Rep. AIAA-2001-2414, June 2001.

[15]Frink, N. T., Pirzadeh, S., Parikh, P., Pandya, M., and Bhat, M., "The NASA Tetrahedral Unstructured Software System," *The Aeronautical Journal*, Vol. 104, No. 1040, Oct. 2000, pp. 491–499.

[16]Anderson, W. K. and Bonhaus, D. L., "An Implicit Upwind Algorithm for Computing Turbulent Flows on Unstructured Grids," *Computers and Fluids*, Vol. 23, No. 1, 1994, pp. 1–22.

[17]Nielsen, E. J., *Aerodynamic Design Sensitivities on an Unstructured Mesh Using the Navier-Stokes Equations and a Discrete Adjoint Formulation*, Ph.D. thesis, Virginia Polytechnic Institute and State University, 1998.

[18]Nielsen, E. J., "An Exact Dual Discrete Adjoint Solution Method for Turbulent Flows on Unstructured Grids," Tech. Rep. AIAA-2003-0272, Jan. 2003.

[19]Mavriplis, D. J., "Multigrid Strategies for Viscous Flow Solvers on Anisotrpic Unstructured Meshes," *Proceedings of the 13th AIAA CFD Conference, Snowmass, CO*, Jun. 1997, pp. 659–675, AIAA Paper 97-1952-CP.

[20]Spalart, P. R. and Allmaras, S. R., "A One-Equation Turbulence Model for Aerodynamic Flows," *La Recherche Aerospatiale*, , No. 1, 1994, pp. 5–21.

[21]Lohner, R. and Parikh, P., "Generation of Three Dimensional Unstructured Grids by the Advancing Front Method," *International Journal of Numerical Methods in Fluids*, Vol. 8, 1988, pp. 1135–1149.

[22]Prizadeh, S., "Three-Dimensional Unstructured Viscous Grids by the Advancing Front Method," *AIAA Journal*, Vol. 34, No. 1, Jan. 1996, pp. 43–49.

[23]Roache, P. J., *Verification and Validation in Computational Science and Engineering*, Hermosa Publishers, 1998.